A magnetic field insensitive graphene transmon qubit

Kian van der Enden

MSc Thesis

Applied Physics, Quantum Nanoscience
Delft University of Technology
Faculty of Applied Sciences
August 18, 2017

Thesis committee:	Prof. dr. ir. Leo Kouwenhoven
	Dr. Leonardo DiCarlo,
	Dr. Michael Wimmer
Supervised by:	James Kroll MPhys

Abstract

Majorana zero modes have been proposed as building blocks of intrinsically fault-tolerant quantum computers. Currently, externally applied magnetic fields are necessary to induce Majorana zero modes in carefully engineered systems. Topological qubit state readout is realized by parity sensing of Majorana islands. However, fast and high fidelity conventional cQED parity readout is incompatible with the magnetic fields needed for Majorana physics. In this thesis, magnetic field insensitive microwave CPW resonators with artificial Abrikosov vortex pinning sites have tested and implemented in a graphene based transmon qubit. It has been shown that these artificial pinning sites reliably trap vortices and are able to retain their zero field $Q_\mathrm{i} \sim 10^5$ up to perpendicular fields of 35 mT. By application of these resonators, we have described the successful continuous wave qubit spectroscopy of a graphene transmon qubit at $B_{||} = 1\,\mathrm{T}$ with a minimal linewidth of 166 MHz and demonstrated manipulation of the qubit frequency between 3.2-7 GHz with electric field. This is the first ever measured superconducting qubit that shows these properties at a magnetic field of 1 T.

Contents

Finis coronat opus

Chapter 1

Introduction

1.1 Topological quantum computer

The race for building the first working and scalable quantum computer is well underway, many research groups and large IT companies (Microsoft [1], Intel [2], Google [3, 4]) from around the world have dedicated expertise and capabilities to this goal. At the heart of the quantum computer is the quantum bit, the quantum brother of the classical building block that powers every computational electronic device in the world. A quantum bit can be realized in many different ways, each with its own (dis)advantages. Leading examples are superconducting transmon qubits with fast gating and readout [5, 6], NV center qubits that have been proven to be a good candidate for quantum communication using optics [7, 8] and spin qubits using electrons [9, 10]. Current problems in the development of a working quantum computer are governed by the loss of information encoded in the qubit due to decoherence. One of the theoretical solutions to this problem was proposed by Nayak et al. using pairs of Majorana particles as qubits that do not suffer from the same decoherence due to its non locality [11, 12]. Because Majorana particles should appear in a topological phase, a quantum computer made up of Majorana particles is called a topological quantum computer. At the same time, Majorana particles exhibit non-Abelian statistics [13], a feat that, whilst exciting in itself, can be exploited to compute with [14, 15].

1.1.1 Majorana computation

The elusive Majorana quasiparticle that is its own antiparticle [16] has, since the first signatures of its existence in 2012 [17], been an increasing topic of interest to use as building block in quantum computation. Majorana quasiparticles are predicted to emerge as bound states at zero energy in 1D or 2D systems that are effectively spinless and superconducting [14]. Due to their existence at zero energy, they are referred to as Majorana zero modes (MZMs), denoted by the symbol $\hat{\gamma}$, are essentially 'half' of a fermion and, vice versa, every fermion can be written in terms of two MZMs.

If we consider a superconducting island with N number of fermions, we are able to count the amount of fermions via the number operator $\hat{n}_i = \hat{c}^\dagger \hat{c}$, where $\hat{c}^\dagger$ ($\hat{c}$) is the creation (annihilation) operator of a fermion expressed in terms of $\hat{\gamma}$ as

$$\hat{c}^\dagger = \frac{1}{\sqrt{2}} \left(\hat{\gamma_1} + i\hat{\gamma_2} \right), \qquad \hat{\gamma_i} = \hat{\gamma_i}^\dagger \tag{1.1}$$

$$\hat{c} \ = \frac{1}{\sqrt{2}} \left(\hat{\gamma_1} - i\hat{\gamma_2} \right). \tag{1.2}$$

If the MZMs do not overlap, we obtain a 2^N-fold degenerate groundstate, because we are in the reference frame of addressing MZMs instead of fermions, so each n_i can still be either 0 or 1. The total of all these fermions, $\sum_{i=1}^{N} n_i$, is either an even or odd number. This even or odd parity is fixed, it can only be changed when a fermion is physically added or removed from the system. This n_i occupation number is the experimentally measurable quantity [14] and when bringing together two MZMs, one can infer from the

energy of the resulting fermionic state if n_i is 0 or 1, i.e. we have measured the parity. To emphasize again, the parity of the whole system is conserved.

Imagine a system with solely one superconducting island on which there are two MZMs which are spatially separated (e.g. on opposite ends of a 1-D nanowire [17]), they effectively still belong to the same fermion but due to the exponential decay of their wavefunction, the overlap is negligible. This spatial separation, together with the superconducting gap, gives them a protection from interaction with local perturbations that couple to fermions, thus are of the form $\gamma_i\gamma_j$. This type of decoherence is suppressed when both MZMs are spatially separated. However, there is one important source of 'decoherence' that *does* influence the usability of MZM as means for quantum computation, the tunneling of a quasiparticle into the system. If an additional quasiparticle is added, the parity of the system has changed and we thus leave the computational subspace we had created, effectively unintentionally resetting the system.

MZMs have the unique property to obey non-Abelian statistics, which means that exchanging MZMs is a non-trivial operation, in contrast with bosons or fermions, where exchange results in a 1 or -1 wavefunction multiplication, respectively. These exchange statistics allow interacting systems of many exchanging MZMs to locally change parity number states, *while always conserving the total parity of the system.* For example, the exchange of γ_2 and γ_3 in a 4 MZM system initially in the $|00\rangle$ parity state results in:

$$B_{23}\,|00\rangle = \frac{1}{\sqrt{2}}\left(|00\rangle + |11\rangle\right), \tag{1.3}$$

where B_{ij} is the exchange (braiding) of γ_i and γ_j. This shows that it is possible for a $|00\rangle$ state to project to a $|11\rangle$ state, which is measurable by measuring both parity numbers. Important to note here is that the parity of the total system is conserved as 0.

In a particular Majorana braiding circuit proposal, several MZMs can be exchanged and used for quantum operations [18,19]. Hyart et al. realize parity measurement with a 'traditional' flux tunable transmon qubit, which is proven to be a fast (sub microsecond resolution) parity sensor [20].

1.1.2 Magnetic field compatibility

So far we have not discussed in which environment MZMs can be engineered, as previously discussed theoretical conditions are not feasible for physical implementation. Therefore in practice, there are several (material) prerequisites needed for the creation of MZMs to approximate the theoretical requirements, among which are the material being an s-wave superconductor with high spin-orbit coupling in a directional (static) magnetic field (of $\sim 0.5\,\mathrm{T}$ for interesting applications) [21–24]. A vast amount of time and resources is being spent on trying to create the perfect environment with grown materials to detect characteristic zero bias peaks [25–27], but in this research we focus on the step after that, incorporating MZMs in a braiding circuit, in which a transmon parity sensor can be a useful readout tool. This does impose the condition that the transmon should be *insensitive to an applied magnetic field.* Unfortunately, the state of the art transmons utilize aluminum which loses its superconducting properties at the strength of the magnetic field we would like to use them in.

1.2 Thesis motivation

We are in search of a magnetic field insensitive transmon, which was initially prompted by the reason described above, to be able to use this for parity readout in a Majorana braiding circuit. At the same time, the spin-qubit community could also gain from having a magnetic field insensitive transmon, as a spin-transmon qubit hybrid system could benefit from the best of both worlds, having long timescale state storage and fast gating, respectively [28]. Furthermore, there is thorough understanding of the transmon following from years of research, which is of great advantage in trying to understand a new type of its kind [6,29,30].

It was chosen to try and produce a transmon with an SNS Josephson junction using graphene as 'normal' metal, from the hypothesis that due to its one-atom thickness the junction should be insensitive to magnetic field, as well as having in-house expertise in contacting single-layer graphene to superconducting leads [31]. There are several more physical reasons for using graphene in an SNS junction, this is discussed in more detail in Section 2.4.8. Choosing graphene had other interesting scientific benefits, as this would be the first

time that graphene would be incorporated in a superconducting qubit system. Furthermore, it could provide an accurate measurement method of the E_J of a graphene Josephson junction.

1.3 The Experiments

The creation of a magnetic field insensitive transmon has other dependencies that are addressed in this thesis. Readout of the transmon state is performed by a superconducting coplanar waveguide resonator, a building block that also has to be made magnetic field insensitive. Recently it has been demonstrated that hole patterning of resonator surfaces makes them insensitive to magnetic fields applied parallel to their surface up to 5.5 T [32].

The research of magnetic field insensitive resonators is continued in this thesis, as we investigate in more detail the performance of resonators with different hole densities in magnetic field. Furthermore, we present measurements and successful qubit spectroscopy of a graphene transmon qubit in $B = 0$ and 1 T, the first of its kind. Finally, measurements of zero-magnetic field Al/AlOx transmons have been performed in order to compare measured E_C values to a FEM simulated result, to increase fabrication accuracy of E_C that can be used for both Al/AlOx and graphene qubits.

The next chapter will discuss superconductivity, Josephson junctions and circuit quantum electrodynamics theory before moving on to transmon theory. Subsequently, we move to the measurement setups for resonator and transmon measurements, after which results of both will be presented and discussed, concluded by E_C measurements and simulations.

It is the author's intention for the reader to enjoy this thesis, it was a privilege to be allowed to produce its content.

Chapter 2

Theory

2.1 Superconductivity

Essential to this research is the metal property called superconductivity. Normal conducting metals have an electrical resistive property that results in energy dissipation when transporting currents through that metal. Some of these metals exhibit the extraordinary property of having *zero* resistivity when the temperature of that metal is below a certain threshold, or critical temperature (T_c), as was discovered first by Kamerlingh Onnes in 1911 [33]. The metal is in that state said to be *superconducting* and the current flowing in a superconductor is correspondingly called the *supercurrent*. A resistance-less conductivity is the first manifestation of superconductivity, but there is an equally important second property of superconductivity. When crossing the critical temperature threshold T_c, externally applied magnetic fields are expelled from the bulk of the superconductor by supercurrents induced just below the surface of the material that exactly cancel the applied magnetic field, called the Meissner effect. This remarkable property will play a vital role in this thesis and we will discuss its influence thoroughly. It was only later that a theoretical insight in superconductivity was developed, and the current understanding stands with what was developed by the London brothers in 1935, Ginzburg and Landau in 1959 and J. Bardeen, L. N. Cooper, and J.R. Schrieffer in 1957, for which the latter company was awarded a Nobel prize. In this chapter we will discuss the origin of superconductivity and the Meissner effect, its implications on DC and AC electrical transport and describe in detail the properties needed to understand the reasoning behind the layout of the devices measured in this thesis. Since its discovery there have been many metals characterized to have a superconducting state all with different critical temperatures, examples are of materials discussed in this thesis are Al with $T_c \sim 1.2\,\mathrm{K}$ and NbTiN at $\sim 15\,\mathrm{K}$.

2.2 Macroscopic superconductivity

Conductivity in normal metals is facilitated by free electrons in its lattice, but in a superconductor something counter-intuitive happens to these electrons. While having the same charge, an attractive interaction takes place below T_c that is large enough to pair up electrons with opposite momentum and spin, called Cooper-pairs. Cooper pairs have, due to this pairing, no momentum nor spin and can thus be classified as bosons. as well, with an energy $>\Delta$. At temperatures sufficiently below T_c, all Cooper-pairs have the same energy of zero momentum and form a Bose condensate, which lowers the ground state E_f of the metal by Δ. This superconducting gap Δ is the energy needed to add a particle to the system that is not a Cooper-pair, a quasiparticle. The density of states (DoS) of a superconductor in comparison with a normal metal is shown in Fig. 2.1, depicting a gap of size 2Δ where no accessible electron states are. Since Cooper-pairs exist because of being in the lowest energy configuration, adding energy to them of 2Δ (e.g. incoming photons) can break the pairs apart and form quasiparticles.

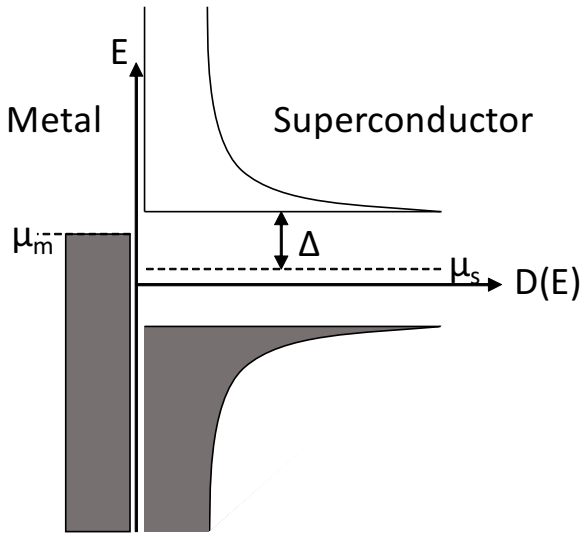

Figure 2.1: Example of a semiconductor description of the density of states (horizontal axis) as function of energy (vertical axis) for a metal with chemical potential μ_{m} (left) in contact with a superconductor with chemical potential μ_{s} (right). The excitation energy of the Bose condensate is 2Δ.

2.2.1 Characteristic parameters

There are several parameters and equations that define a superconductor, linked to its defining properties such as the superconducting gap and the Meissner effect.

2.2.1.1 Coherence length

The coherence length ξ_0 is the length over which the superconducting state (of a Cooper-pair) is preserved. This is an important length scale to consider in situations where superconductivity is broken, e.g. at boundaries with normal metals. In BCS theory the coherence length is defined as

$$\xi_0 = \frac{\hbar v_{\mathrm{f}}}{\pi \Delta}, \tag{2.1}$$

where v_{f} is the Fermi velocity and Δ the known superconducting gap at 0 K [34].

2.2.1.2 Penetration depth

The Meissner effect describes the expulsion of the magnetic field from the bulk, but there is always a certain portion of the outer part of a superconductor penetrated with the field. The penetration depth is therefore the lengthscale of the penetration of magnetic field in a superconductor, which is defined from the London equations as

$$\lambda_L = \sqrt{\frac{mc^2}{4\pi n_{\mathrm{s}} e^2}}, \tag{2.2}$$

with n_{s} the density of Cooper-pairs, m the electron mass, at $T = 0\,\mathrm{K}$ [34]. The density of Cooper-pairs is temperature dependent, where $n_{\mathrm{s}} \to 0$ for $T \to T_c$, resulting in a diverging λ_L, which corresponds to the superconductor becoming a normal metal again.

2.2.2 Type-II superconductors

So far we have acknowledged only type-I superconductors, those that expel magnetic fields up to a certain critical field B_c, after which the superconductivity breaks down and magnetic fields are free to travel through the metal. Defined by the Ginzburg-Landau parameter $\kappa = \lambda/\xi_0$, superconductors with $\kappa > 1/\sqrt{2}$ fall in the category of type-II, being characterized by an intermediary regime where fluxlines penetrate the superconductor in an ordered fashion for fields $B_{c1} < B < B_{c2}$, the Schubnikov phase. The penetrating fluxlines have magnitude of one flux quantum $\Phi_0 = \frac{h}{2e}$, that locally have destroyed superconductivity and thus exist in an area where the Cooper-pair density is zero. The flux is mediated by an Abrikosov *vortex* of supercurrent of size ξ_0, circling around the center of the flux penetration area, focusing the flux towards the center of the vortex [35].

2.2.2.1 Vortex statics and dynamics

In sufficiently high magnetic field, vortices order themselves in a lowest energy configuration due to repulsive interaction of neighboring vortices. It has been found that this structure is a triangular lattice [34], with lattice constant

$$a_0 = \left(\frac{2}{\sqrt{3}}\right)^{1/2} \sqrt{\frac{\Phi_0}{B}}, \tag{2.3}$$

where the magnetic field dependence of the density of vortices becomes apparent. When only few vortices are present in a type-II superconductor in a small magnetic field close to T_c, vortices are free to move and are not limited by restoring lattice forces as result of vortex interaction. Vortices will experience dynamical forces due to any directional (super)currents in the superconductor they are present in (e.g. current biasing a superconducting strip). This is described by the Lorentz force per unit length of the vortex $\mathbf{f_L}$ due to a current density $\mathbf{J}$ as

$$\mathbf{f_L} = \mathbf{J} \times \mathbf{\Phi_0}, \tag{2.4}$$

where $\mathbf{J}$ interacts with the flux quantum the vortex trapped. For a high density of vortices the Lorentz force density can be written as

$$\mathbf{f} = \mathbf{J} \times \mathbf{B}. \tag{2.5}$$

As these supercurrent vortices move with velocity $\mathbf{v}$ due to the Lorentz force, they induce an electric field

$$\mathbf{E} = \mathbf{B} \times \mathbf{v}, \tag{2.6}$$

which is oriented in the same direction as the applied current. Since the vortex moves with its normal-metal core, a dissipation in the superconductor is present which damps the vortex motion with the flux flow resistance ρ_{ff} defined as [36]

$$\rho_{\mathrm{ff}} = \frac{|\mathbf{E}|}{|\mathbf{J}|}. \tag{2.7}$$

2.2.2.2 Vortex (de-)pinning

So far only an ideal type-II superconductor has been regarded where, if only few vortices are present, they are allowed to move around freely. In reality, vortices tend to nucleate at certain locations on the material where superconductivity is weaker, such as grains, holes or defects, which are present in almost all artificially created films. It is energetically favorable for the vortex to be created in a region where quasiparticle excitations are already present. That results in the vortex to be 'pinned' to that energy well. Hopping out of this well can occur, e.g. by thermal excitation, at a rate defined by Boltzmann statistics to overcome the threshold U, expressed in hopping time t as

$$t = t_0 e^{U/kT}, \tag{2.8}$$

what is t_0 and the Boltzmann constant k [37]. This rate is enhanced when a current is applied, for there is the additional Lorentz force pulling on the vortex. We can model this by assuming the barrier U becomes $|\mathbf{J}|$-dependent as

$$U(J) = U_0 \left(1 - \frac{J}{J_c}\right), \tag{2.9}$$

where we define $J = |\mathbf{J}|$, J_c as the critical current density and U_0 as the potential barrier when no Lorentz force is present. We can then combine Eq. 2.8 and 2.9 to obtain the Anderson-Kim flux creep equation [38]

$$J = J_c \left[1 - \frac{kT}{U_0} \ln \left(\frac{t}{t_0} \right) \right]. \tag{2.10}$$

Separately from temperature dependence of vortex depinning we can regard the movement of vortices whilst pinned, due to the acting Lorentz force. This can be viewed as the vortex being in a one-dimensional potential well, where the confinement potential $U(x)$ acts as a counter force for the externally applied Lorentz force, as the vortex is assumed to only move from the pinning site at a certain large enough force. Since this pinning site is of finite size, the vortex is allowed to oscillate within this site, following the equation of motion

$$\eta \dot{\mathbf{x}} + k_p \mathbf{x} = \mathbf{F_L}, \tag{2.11}$$

assuming that the potential can be regarded as a harmonic oscillator with spring constant k_p and where η is the dampening term due to the flux flow resistance. Solving this differential equation leads to the characteristic depinning frequency $\omega_d = k_p/\eta$ [39, 40]. For applied frequencies $\omega > \omega_d$ the impedance of the system becomes the impedance of the 'ideal' mixed state, where vortices are depinned and sloshed around with a flux flow resistance dampening, thus dissipating energy. If the applied energy is $\omega < \omega_d$, the vortices stay pinned and their contribution to the total impedance is zero, making currents flow without resistance.

2.2.2.3 Controlled vortex pinning

It is possible to control the nucleation of vortices, either by changing the geometries such that no vortices are created in a particular region, or by intentionally trapping vortices at nucleation in (deep) potential wells such that the chance of being excited out of that well is small.

In the first situation we would need to use narrow strips of superconductor. We consider such a sheet of type-II superconductor of finite thickness t, width W and length $L \gg W$ where an in-plane magnetic field B is applied, which penetrates the superconductor with the Pearl length $\Lambda = 2\lambda^2/t$. When we take $W < \Lambda$ at a temperature $T \simeq T_c$, the sheet is fully penetrated by many quasi-free fluxoids. When the temperature is lowered the pinning potential of the vortices dominates over their thermal energy and they freeze at a location in the sheet that is determined by the resultant of an image force[1] and screening current[2] [41, 42].

Vortex pinning for a larger surface of superconducting film requires the second option of vortex control, intentional trapping with artificial potential wells. These artificial pinning sites are lithographically defined holes in a superconducting film, which makes it a scalable approach. The supercurrent of the vortex rotates around the 'hole' without having to spend energy on breaking Cooper pairs for its 'normal' core. This makes it energetically favorable for the vortex to sit in the artificial defect whilst experiencing a corresponding restoring force pinning it into the defect [43]. This method has been demonstrated to have a small but consistent improvement in resilience to perpendicular magnetic fields [44].

2.2.3 Thin film superconductors

The behavior of superconductors in magnetic field depends on size parameters of the material. In planar geometries, the thickness of the film is an important measure for magnetic field penetration. The thinner the film becomes, the easier it is for fieldlines perpendicular to penetrate the superconductor, especially when regarding films with a thickness $t < \lambda_L$. However, thinner films are very resilient against parallel applied magnetic fields, as has been measured for e.g. Al [45]. Films with $t \sim \xi$ will have low probability

[1] The boundary condition of zero perpendicular surface current on the sides of the sheet result in the creation of an image vortex with a mirrored direction of the current. The force between the so called anti-vortex and vortex is attractive, which results in the vortex being pulled to the sides of the sheet.

[2] Even though $W < \Lambda$, an applied magnetic field does not result in a uniformly distributed B in the sheet, but decreases symmetrically and exponentially to $W/2$. The resulting screening Meissner currents create a *repulsive* B field to the fluxoid if they are in the *same* direction and *attractive* for *opposite* direction with respect to each other. This results in the vortex moving towards $W/2$ or to the sides, respectively. In the former this force competes with the image force, whereas it acts constructively in the latter. The repulsive force is proportional to B and thus shall always overcome the image force for sufficiently high B, expelling all vortices from the film (one can imagine reversing the magnetic field after the vortices have been frozen to a location in order to move them).

of having vortices in the parallel-to-film direction, as vortices are of size $\sim \lambda_L$ and thus will require higher magnetic field energy to overcome the barrier this imposes on the vortex creation. Experiments confirmed an analytical description for the critical field parallel field of thin-film superconductors to be [42, 46]

$$B_{c,1} = \frac{1.65\Phi_0}{t^2}, \tag{2.12}$$

2.2.4 High frequency properties of superconductors

When regarding DC current, the lossless conduction is mediated by Cooper pairs. The conduction of a superconducting metal at temperature $T \ll T_c$ is not necessarily infinite when an alternating current is applied to it, as is the case in this thesis. Sending microwave photons through a superconductor is an example of high-frequency alternating current of the GHz order. Since quasiparticles exist for $T \neq 0$, a frequency dependent resistivity is ever present due to moving quasiparticles and additionally from breaking Cooper pairs (in coalition with thermal excitation). This introduces minor losses that together form a energy drain for e.g. superconducting resonators. Together with the Drude model for normal metal conduction with electrons and from the London equations for Cooper pairs, we can describe conduction in a superconductor in the *two fluid model* [47].

2.2.4.1 Two-fluid model

We will regard two flows of current, one by the flowing of Cooper pair density n_s with effective mass $m_\mathrm{s}^\star$ and charge $q^\star$ and the other by the flowing of quasiparticle density n_n with $m_n^\star$ and e as effective mass and charge, respectively.

2.2.4.1.1 Drude model

From the normal current density $\mathbf{J_n} = n_n e \mathbf{v_n}$, with $\mathbf{v_n}$ the average velocity of the quasiparticles, the equation of motion can be written in terms of Newton's second law applied to charges in an electric or magnetic field

$$\frac{d\mathbf{p}}{dt} = -\frac{\mathbf{p}(t)}{\tau} + \mathbf{F_{em}} = \mathbf{F_{em}} + \mathbf{F_d}, \tag{2.13}$$

where τ is the average time between two scattering events of the quasiparticles, which is expressed as a 'drag' term, $\mathbf{F_d}$. We express the electromagnetic force as the Lorentz force $\mathbf{F_{em}} = e\left(\mathbf{E} + \mathbf{v} \times \mathbf{B}\right)$ and since we assume $B = 0$ inside a superconductor, we are left with

$$m_n^\star \left(\frac{d\mathbf{v_n}}{dt} + \frac{\mathbf{v_n}}{\tau} \right) = e\mathbf{E}. \tag{2.14}$$

We can write a sinusoidal current drive $\mathbf{E}(t)$ and electron response $\mathbf{v}(t)$ as

$$\mathbf{E}(t) = \mathrm{Re}\left[\mathbf{E}(\omega) e^{\imath\omega t}\right], \tag{2.15}$$

$$\mathbf{v}(t) = \mathrm{Re}\left[\mathbf{v}(\omega) e^{\imath\omega t}\right]. \tag{2.16}$$

Substituting both relations into Eq. 2.14, rewriting back to $\mathbf{J_n}$ and using Ohm's law gives the frequency dependent quasiparticle conductivity

$$\sigma_n(\omega) = \frac{\mathbf{J_n}(\omega)}{\mathbf{E}(\omega)} = \left(\frac{n_n e^2}{m_n^\star} \right) \frac{\tau}{1 + \imath\omega\tau}. \tag{2.17}$$

2.2.4.1.2 Superfluid conductivity

Using the first London equation

$$\frac{\partial \mathbf{J_s}}{\partial t} = \frac{n_\mathrm{s}^\star q^{\star 2}}{m_\mathrm{s}^\star} \mathbf{E} \tag{2.18}$$

and applying Eq. 2.15 and 2.16 in the same fashion as we did for the Drude model, we obtain

$$\imath\omega\Lambda\mathbf{J_s} = \imath\omega\mu_0\lambda_L^2\mathbf{J_s} = \mathbf{E}, \tag{2.19}$$

using the known London penetration depth and London coefficient λ_L and $\Lambda = m_s^\star / n_s^\star q_\star^2$, respectively. Rewriting this equation gives us the purely imaginary conductivity of the superfluid

$$\sigma_s = \frac{n_s^\star q_\star^2}{\imath \omega m_s^\star} = \frac{1}{\imath \omega \Lambda} \tag{2.20}$$

Together, Eq. 2.17 and 2.20 represent the total conductivity of a superconductor,

$$\sigma = \sigma_n + \sigma_s = \sigma_1 - \imath\sigma_2 = \frac{n_n e^2 \tau}{m_n^\star} - \imath \frac{n_s q^{\star 2}}{\omega m_s^\star}, \tag{2.21}$$

where we have taken the assumption that $\omega\tau \ll 1$. This corresponds to $\hbar\omega \ll \Delta$ and $T \ll T_c$, which allows certain terms to be dropped, simplifying the expression. It is instructive to note that for superconductors with Δ of $\sim 1\,\text{meV}$ (as is the case for NbTiN) the corresponding $\Delta/\hbar \approx 1\,\text{THz}$, which is indeed well above microwave frequencies and our approximation holds. If that would not have been the case, we would have had to invoke the Mattis-Bardeen equations, which are considerably harder to work with due to their complexity [47].

2.2.5 Kinetic inductance

Where there is current flowing, magnetic fields are generated as well. In those fields energy is stored, as is in the particles mediating the current (electrons, Cooper pairs) in the form of kinetic energy. Changing magnetic field or velocity vector has a certain timescale associated with it, either due to Lenz's law for the magnetic field, or due to the property of inertial mass in the current carriers. This magnetic and kinetic inductance together can be expressed in the scalable parameter of surface resistance R_s and surface inductance L_s, and thus as surface impedance $Z_s = R_s + \imath X_s$, respectively defined as

$$R_s = \frac{1}{2}\omega^2 \mu_0^2 \lambda_L^3 \left(\frac{e^2}{m_n^\star}\right) n_n, \tag{2.22}$$

$$X_s = \imath \omega \mu_0 L_s, \tag{2.23}$$

where $L_s = \mu_0 \lambda_L$ is the surface kinetic inductance. We see R_s diminishes for $n_n \ll 1$, which we expect to occur when $T \ll T_c$ as then the amount of quasiparticles in the system is small, which makes X_s the dominating factor of impedance for a superconductor.

2.3 Nonlinearity: Josephson junctions

Postulated in 1962, Brian Josephson predicted the voltage and current relation between two superconductors connected via a weak link. This weak link can be anything that locally restricts superconductivity, such as a normal metal sandwiched between two superconductors (SNS, superconductor - normal metal - superconductor), or an insulating barrier (SIS), even a constricting piece of superconductor (ScS). He realized a supercurrent I_s could tunnel through this weak link, without dissipation, driven by the macroscopic quantum phenomena of the difference in (macroscopic) phase $\Delta\phi$ between the two superconductors, otherwise known as the Ginzburg-Landau complex order parameter. This supercurrent is defined as

$$I_s = I_c \sin(\Delta\phi), \tag{2.24}$$

where I_c is the critical current, the maximum allowable supercurrent through the weak link before a voltage drop occurs, making the system dissipative. It is possible to change $\Delta\phi$ by applying a voltage difference between the two SCs, which time evolves the phase as

$$V(t) = \frac{\hbar}{2e}\frac{\partial\phi}{\partial t}. \tag{2.25}$$

For a constant voltage, the supercurrent therefore oscillates with frequency $\omega = 2eV/\hbar$. Together, Eq. 2.24 and 2.25 make up the two characteristic equations that represent the Josephson effect. Next, we have to redefine the phase difference to be gauge-invariant. With the current definition of $\Delta\phi$, it is not possible to determine the phycial quantity I_s properly because $\Delta\phi$ does not have a unique value for a certain physical situation. Introducing the gauge-invariant phase difference γ as

$$\gamma \equiv \Delta\phi - \frac{2\pi}{\Phi_0}\int \mathbf{A}\cdot d\mathbf{l}, \tag{2.26}$$

integrating the magnetic vector potential $\vec{A}$ over the totality of the weak link. The useful supercurrent relation then becomes

$$I_s = I_c \sin(\gamma). \tag{2.27}$$

2.3.1 RCSJ model

Although a physical Josephson junction for finite voltages does behave as ideally as Eq. 2.27, there are electrode capacitances and resistance from the contacts.

The RCSJ (resistively and capacitively shunted junction) takes these parameters into account, whilst retaining the ideal JJ at its heart. An ideal JJ is shunted with both a voltage dependent resistance R as well as a capacitance C, as shown schematically in Fig 2.2. If we apply Kirchoff's law to this circuit we equate the applied bias current I to the contributions from the three channels

$$0 = I_c \sin\gamma + \frac{V}{R} + C\frac{dV}{dt} - I. \tag{2.28}$$

When we then substitute V using Eq. 2.25, using the gauge-invariant phase difference, to obtain

$$0 = I_c \sin\gamma - I + \frac{\hbar}{2eR}\frac{\partial\gamma}{\partial t} + \frac{\hbar C}{2e}\frac{\partial^2\gamma}{\partial t^2} \tag{2.29}$$

In this we recognize the equation of motion for a particle in a damped harmonic oscillator

$$0 = \frac{\partial U}{\partial\gamma} + D\frac{d\gamma}{dt} + m\frac{d^2\gamma}{dt^2}, \tag{2.30}$$

in which the driving force is from the differentiation of the potential U , the dampening D and mass of the particle m, defined by

$$\begin{cases} U(\gamma) & = -\frac{\hbar}{2e}\left(I_c\cos\gamma + \gamma I\right) \\ D & = \frac{1}{R}\left(\frac{\hbar}{2e}\right)^2 \\ m & = C\left(\frac{\hbar}{2e}\right)^2. \end{cases} \tag{2.31}$$

Note the multiplication of a factor $\left(\frac{\hbar}{2e}\right)$ to Eq. 2.30 to obtain the definitions above. We can simplify $U(\gamma)$ by introducing the **Josephson coupling energy** $E_J = I_c\hbar/2e$, the energy stored in the junction because of the overlap in macroscopic wavefunctions of the two superconductors. This is a characteristic value we will encounter many times involving qubits. Furthermore we can define a frequency to the oscillation of the particle being in a well, the plasma frequency

$$\omega_p = \sqrt{\frac{2eIc}{\hbar C}}. \tag{2.32}$$

Corresponding to that, the quality factor Q_J of the oscillation

$$Q_J = \omega_p RC, \tag{2.33}$$

where the system is underdamped or overdamped for $Q \gg 1$ or $Q \ll 1$, respectively.

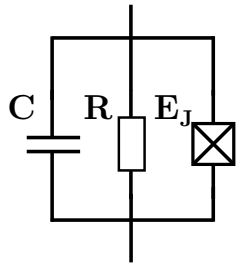

Figure 2.2: The RCSJ model schematically in a circuit diagram, a Josephson junction is shunted to both a resistance and capacitance.

2.3.2 Tilted washboard potential

The potential $U(\gamma)$ is also known as the 'tilted-washboard potential', since an analogy can be made to a particle of mass m moving along the γ axis in the potential $U(\gamma)$, see Fig. 2.3. Initially, for $I < I_c$, this particle gets trapped in a potential well and has a constant γ (at $T = 0\,\mathrm{K}$). Then, for increasing I, the washboard tilts downwards until the particle is able to 'run down' without being retrapped in another well, this is when $I \geq I_c$. This is analogous to the two states the JJ has: Firstly, having a constant γ, from which follows that no voltage difference will appear for $I < I_c$. Secondly, for $I \geq I_c$ a voltage difference and dissipative state occurs due to the time evolving γ (see Eq. 2.25). It can be noted that γ is not always constant in the region $I < I_c$, for thermal excitation can result in our imaginary particle being kicked out of its well into another, thereby changing γ.

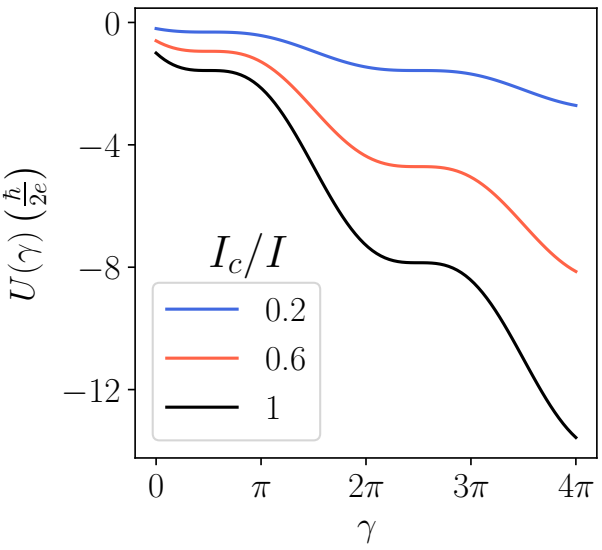

Figure 2.3: The tilted washboard potential of Eq. 2.31 for three different values of the I_c/I ratio, where see the potential tilt downwards for increasing I_c/I ratio.

2.3.3 SNS Josephson junction

Supercurrent transport from a normal metal (conduction with electrons or holes) to a superconductor (Cooper pairs) is mediated by incoming electrons/holes from the normal metal on the N-S interface to be reflected with equal but opposite momentum as hole/electron, effectively creating a Cooper pair in the superconductor. This process is schematically depicted in Fig. 2.4. The process of current carriers reflecting of the N-S interface is called 'Andreev reflection', and appropriately the state of the wavefunction describing the transport in the normal metal is called the 'Andreev bound state' (ABS).

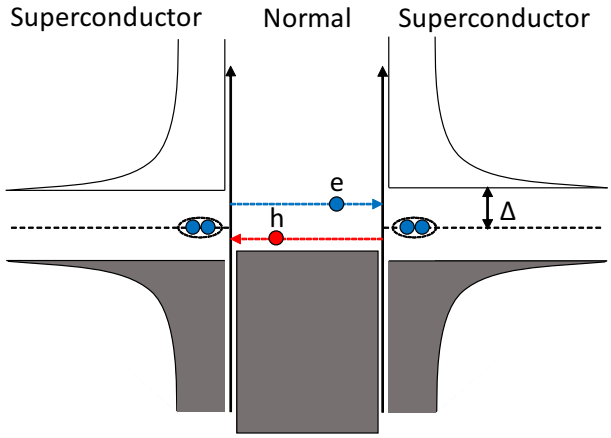

Figure 2.4: A schematic representation of the process of current being transported from one superconductor to another through a normal metal, by means of an Andreev bound state.

The total phase acquired during one cycle of the ABS has to be a multiple of 2π. This total phase depends on the phase difference between the two superconductors γ, the wavevectors of the hole and electron $\mathbf{k}_\mathrm{h}, \mathbf{k}_\mathrm{e}$ and the phase difference defined by the the reflection of the hole or electron, which is described by $\arccos \frac{E}{\Delta}$, where E is the energy of the hole or electron. The total phase is then the summation of these parameters,

$$\gamma + (\mathbf{k}_\mathrm{e} - \mathbf{k}_\mathrm{h})\, L - 2 \arccos \frac{E}{\Delta} = 2\pi n. \tag{2.34}$$

Analytical solutions for the number of energy levels as well as the current-phase relation (CPR) through the junction exist for SIS junctions in both the short and long junction limit. For SNS junctions, these analytical solutions exist for a single channel, long junction 1D nanowire [48, 49]. The SNS Josephson junction used in this thesis is intermediary in terms of junction length and amount of conduction channels. In this regime, no analytical solutions exist for the energy levels nor for the CPR. However, we do not need such a description to intuitively understand how the supercurrent depends on the state of the normal metal.

As the amount of current carriers in the metal is increased (either by more electrons or more holes), the number ABSs should increase as well, especially when we are not confined to a single conduction channel. That means that when a gate voltage is applied to the normal metal and the current carrier density is increased, so should the amount of current through the junction, i.e. the amount of energy contained in the junction, the Josephson energy E_J, will also increase.

2.4 cQED

Before we move into transmon theory we must take a step back and understand the framework in which the transmon operates, using frequencies in the RF spectrum and superconducting circuits, named circuit Quantum Electrodynamics (cQED), the solid state version of Cavity Quantum Electrodynamics (CQED).

The circuit implementation of cQED used in this thesis employs 2D superconducting coplanar waveguides (CPWs) that carry microwaves via an oscillating electric field between the center pin and ground plane, a 2D version of a coax geometry. In the same fashion as atoms couple to photon modes in cavities in a CQED system [50–52], cQED cavities (resonators) exist by creating CPW transmission lines of a certain length in which resonant microwaves live for a certain amount of time. It is possible to address (several) resonators from one single transmission line using capacitive coupling. In the following sections the theory behind transmission lines and resonators relevant to this thesis will be given, such that we understand the circuitry which allows us to measure qubits.

2.4.1 Transmission lines

The key tool to guide our microwaves is a transmission line, in our case a center strip that capacitively couples to the ground next to it, as shown in Fig. 2.5. We can, however, model such a transmission line independent of its type of implementation. The impedance Z_0 of the totality of the transmission line can be expressed in the elements of the circuit R_l, L_l, G_l, C_l, all per unit length, which are resistance, inductance, conductance and capacitance, respectively. The R_l represents the resistance due to the finite conductivity of the conductors, and the shunt conductance G_l is the leakage to the dielectric that is between the conductors, silicon or sapphire, in our case (see Fig. 2.5). There is, as stated before, a capacitance between the center line and the ground, which is C_l, leaving L_l as the total inductance of the conductor, well explained in the previous section on superconductors. Following from the differential equation of applying Kirchhoff's law we obtain

$$Z_0 = \sqrt{\frac{R_l + j\omega L_l}{G_l + j\omega C_l}} \approx \sqrt{\frac{L_l}{C_l}},^{3} \tag{2.35}$$

where the approximation can be made if the loss in the system is small (as usually is the case for superconductors). As signals on a transmission line propagate as a wave, they have a propagation coefficient γ_p which reminds us of Z_0 as $\gamma = \sqrt{(R_l + j\omega L_l)(G_l + j\omega C_l)}$. The phase velocity of the wave is defined as $\nu = \omega/\theta_w$, where $\theta_w = \mathrm{Im}[\gamma]$ is the phase of the wave. In the nearly lossless case the phase velocity is then

$$\nu \approx \sqrt{\frac{1}{L_l C_l}}, \tag{2.36}$$

with a wavelength

$$\lambda = \frac{2\pi}{\omega\sqrt{L_l C_l}} \tag{2.37}$$

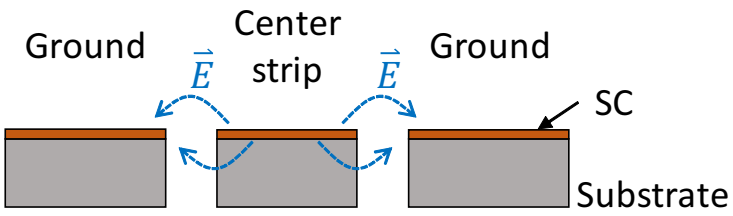

Figure 2.5: Schematic drawing of a CPW transmission line, capacitively coupled to the ground plane next to it.

[3]Note that we use j as imaginary number, which is common in electrical engineering. This relates to our quantum imaginary $\imath = -j$

2.4.2 Coplanar waveguides

We must now let go of our general description of the circuit elements, because geometry and physical implementation of these elements will alter some of the general formulas. As mentioned, resonators and transmission lines are realized by Coplanar Waveguides (CPWs) with a center strip of width w and gap to the ground plane d, both values are typically $\sim$ µm. Electric and magnetic field lines between the center strip and the ground plane are perpendicular to the direction of propagation, with currents flowing at the edges of the center strip and ground plane, in opposite direction of each other. Devices used in this thesis have CPWs made from a NbTiN film on either silicon or sapphire substrates. As such, an effective dielectric constant ϵ_{eff} has to be used, as half of the field lines pass through the substrate and the other through vacuum. By approximation for a substrate of infinite thickness, we can define

$$\epsilon_{\text{eff}} \approx \frac{1 + \epsilon_{\text{substrate}}}{2}. \tag{2.38}$$

We want to achieve impedance matching to the measurement equipment to prevent signal reflection, thus we aim for $Z_0 = 50\,\Omega$, which we can calculate using Eq. 2.35, however both L and C depend on the geometry of the CPW. The inductance has two contributions, the geometric magnetic and kinetic inductance, where $L = L_k + L_m$. We define the capacitance and L_m per unit length as

$$L_m = \frac{\mu_0}{4}\frac{K(k')}{K(k)}, \tag{2.39}$$

$$C = 4\epsilon_0\epsilon_{\text{eff}}\frac{K(k)}{K(k')}, \tag{2.40}$$

where K is the complete elliptic integral of the first kind and

$$k = \frac{w}{w + 2d}, \tag{2.41}$$

$$1 = k^2 + k'^2, \tag{2.42}$$

using the geometry of the CPW with the stripline width w and gap d. For the kinetic inductance per unit length we can use the definition for L_k of a superconductor, with a geometrical factor $g(d, w, t)$ found by Yoshida et al. by using the conformal mapping technique [53]

$$L_k = \frac{\mu_0\lambda^2}{wt}g(d, w, t). \tag{2.43}$$

with the geometrical factor given by

$$g(d, w, t) = \frac{1}{2k^2K(k)^2}\left(-\ln\left(\frac{t}{w}\right) + \frac{2\,(w + d)}{(w + 2d)}\ln\left(\frac{d}{w + d}\right) - \frac{w}{w + 2d}\ln\left(\frac{t}{4\,(w + 2d)}\right)\right). \tag{2.44}$$

This factor is weakly dependent on t and w, thus L_k decreases with increasing cross sectional area $S = wt$. As we have done in general for superconductors, we have assumed that $t < \lambda$ which ensures us that the current distribution is uniform.

Qualitatively we can summarize the above equations that the kinetic inductance changes with the thickness of the superconducting film, thus changing the resonance frequency (as we will see in Eq. 2.46) which is a consequence that has to be taken into account with fabrication.

2.4.2.1 $\lambda/4$ resonators

In this thesis $\lambda/4$ resonators are used, chosen because of their short length and compatibility with a multi-resonator and qubit chip. The resonators are built from CPW that are open on one and shorted on the other end, where the resonance frequency is given by

$$\omega_0 = \frac{2\pi}{4l\sqrt{(L_m + L_k)C}}, \tag{2.45}$$

where l is the resonator length, and L_m, L_k and C defined as above. Resonators are designed to be in the microwave spectrum, usually between 3-8 GHz. The resonance frequency depends on L_k, which in turn is inversely proportional to the density of Cooper pairs. Any change in Cooper pair density n_s by e.g. an incoming photon will therefore influence the resonance frequency, which is why superconducting resonators are also used as photon detectors [54]. The change in resonance frequency as a function of change in kinetic inductance is given by [55]

$$\frac{\partial \omega_0}{\omega_0} = -\frac{\alpha}{2}\frac{\partial L_k}{L_k}, \tag{2.46}$$

which is necessary to know for our evaluation of resonators in an applied magnetic field. In this equation $\alpha = \frac{L_k}{L_m + L_k}$, defined in the previous section. In our case a sudden change in L_k is a source of noise, any thermal or photon excited breaking of Cooper pairs will broaden the resonance peak obtained when frequency probing it.

2.4.3 Resonator coupling

All resonators on a device are capacitively coupled to the transmission line, or feedline, with an elbow arm on the open end. Changing the dimensions of this arm and the distance between the resonator and the feedline will influence the coupling strength between the two. The rate at which photons transfer from resonator to feedline (or vice versa) is defined as the coupling quality factor Q_c, which is a specific application of the quality factor

$$Q = \frac{\omega E}{P}, \tag{2.47}$$

that expresses the current energy in the system E over the energy lost per cycle ω/P. For clarity, a higher quality factor means a lower rate of energy exchange. The combined quality factor that incorporates all losses is called the *loaded* quality factor, Q_l. It is related to Q_c, since this is one port of loss, and the so called *internal* quality factor Q_i that takes all internal resonator losses into account, given by

$$\frac{1}{Q_l} = \frac{1}{Q_c} + \frac{1}{Q_i}. \tag{2.48}$$

Internal losses can be losses due to quasiparticles, dielectric, interaction with vortices, incoming radiation or two-level systems (TLS) in the substrate. Controlling these factors is important when trying to achieve high Q_i resonators [56].

2.4.4 Resonator fitting

In this thesis resonators have been measured by reading out the amplitude and phase of the transmission, which requires phase locking in the setup when one wants to sweep the input frequency, see Chapter 3. This resonance is fit in the real-complex plane according to the *'hanger function'*. The input/output relation of the transmission line is defined as $S_{21} \equiv V_\mathrm{out}/V_\mathrm{in}$. Below the fitting function and its dependencies are explained.

2.4.4.1 Hanger function

The complex transmission S_{21}^* can be derived from applying Kirchoff's law to the transmission system, taking into account impedance mismatching from the source/drain to and from the resonator, as performed by Khalil et al. [57]. This results in

$$\mathrm{S}_{21}^* = A\left(1 - \frac{\frac{Q_l}{|Q_e|}e^{i\theta}}{1 + 2\imath Q_l \frac{\omega - \omega_0}{\omega_0}}\right), \tag{2.49}$$

with ω the input frequency, ω_0 the resonance frequency of the resonator and A the diameter of the resonance circle, which is equal to the width of the 3dB-point of the $|S_{21}|$. Resonators with an impedance mismatch, as described in this thesis, have a characteristic asymmetrical transmission line shape. The asymmetry of

the hanger is quantified by θ, the rotation angle of the resonance circle around the off-resonance point. Also an external quality factor has been introduced, Q_e, that is related to the coupling by

$$Q_e = Q_c \cos\theta. \tag{2.50}$$

Eq. 2.49 does not take into account the propagation phase difference ϕ_v due to the microwave traveling to and from the resonator in the feedline, which results in moving on the edge of a circle around the origin in the real-complex plane. Also, the transmission of the feedline is not constant with changing frequency ω, which can be taken into account using a first order approximation. Taking these conditions and plugging them into Eq. 2.49 results in

$$\mathrm{S}_{21} = A\left(1+\eta\frac{\omega-\omega_0}{\omega_0}\right)\left(1-\frac{\frac{Q_l}{|Q_e|}e^{i\theta}}{1+2iQ_l\frac{\omega-\omega_0}{\omega_0}}\right)e^{i(\phi_v(\omega-\omega[0])+\phi_0)}, \tag{2.51}$$

where the $\omega-\omega[0]$ term is there to uncorrelate the first guess of ϕ_v and ϕ_0 in the fit that will be performed on the experimental data points using this function and η allows a linear variation in the overall transmission chain in the narrow frequency range around any given resonance [56]. This is considered to be *the* hanger function.

2.4.5 Photon number

Resonator-qubit interaction takes place in the single-photon regime. The input power P_in of the microwaves that enter the resonator that has internal power P_int should reflect this single-photon regime. We can relate the input and internal power by

$$P_\mathrm{int} = \frac{2}{\pi}\frac{Q_l^2}{Q_c}P_\mathrm{in}, \tag{2.52}$$

that together with the definition of average photon number occupation

$$\langle n_{ph}\rangle = \frac{\pi P_\mathrm{int}}{\hbar\omega^2} \tag{2.53}$$

will form [58]

$$\langle n_{ph}\rangle = \frac{4}{\hbar\omega^2}\frac{Q_l^2}{Q_c}P_\mathrm{in}. \tag{2.54}$$

2.4.6 $\lambda/4$ resonators in parallel magnetic field

Thin film superconducting resonators are known to be able to withstand several 100 mT of parallel magnetic field, but are known to become unusable at higher fields due to vortices draining the resonator energy. To improve the magnetic field compatibility either the geometries have to be constrained, or artificial pinning sites have to be introduced (as discussed in Section 2.2.2.3). The first option has been researched by Samkharadze et al., who used NbTiN nanowires that have $Q_i > 2\cdot10^5$ at parallel applied magnetic field of $B_{||} = 6\,\mathrm{T}$.

Introducing artificial pinning sites has recently been used inside the center strip of the CPW resonators by Borsoi [32]. He showed initial results of $Q_\mathrm{i} \sim 10^6$ up till $B_{||} = 5.5\,\mathrm{T}$. Both researches showed a change in resonance frequency $\partial f_r/f_r = -k||B_{||}^2$, with $k_{||}$ a fitting coefficient, which reflects the change in L_k due to the increased breaking of Cooper pairs as the magnetic field penetrates the film more.

2.4.7 cQED: From atom to qubit

The analogous atom in the cQED framework, is in fact an artificial atom, a qubit. A cQED qubit can be realized in many ways [59], but a proven implementation is the so called charge insensitive qubit named Transmon [29], a qubit derived from the Cooper-pair box [60]. Together the CPW resonator and Transmon qubit form the cQED equivalent of the atom-photon interaction in CQED, that can be characterized by the interaction strength g and atom cavity detuning Δ due to capacitative coupling of the resonator and qubit [61]. The qubit-resonator system operates in the 'dispersive' regime, where $|\Delta| \gg g$ [62].

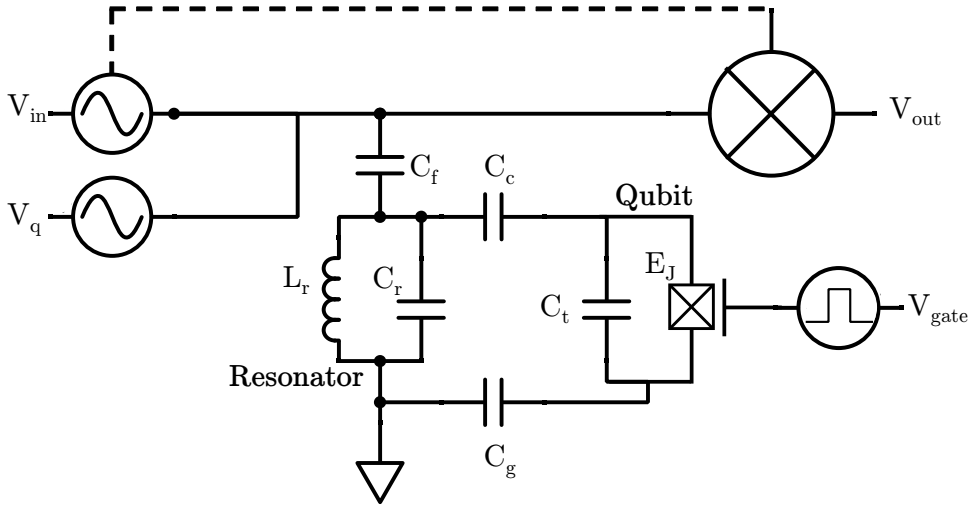

Figure 2.6: Schematic circuit diagram of the resonator-qubit system attached to the readout and control system. The transmission between the RF signals V_{in} and V_{out} is measured, and when addressing the qubit an additional V_q is added as RF source. Note that the Josephson junction is gated instead of flux coupled.

2.4.7.1 Transmon qubit

The transmon is a qubit that uses the same Josephson junction layout as a Cooper pair box (CPB), but has a shunted capacitor in addition to the present coupling to the CPW resonator (an LC oscillator), as shown in Fig. 2.6. When the transmon was introduced by Koch et al. [29] it made use of a dc-SQUID with externally flux Φ tunable Josephson energy E_J, which for identical Josephson junctions can be described by $E_J = E_{J,max} \left|\cos\left(\pi\Phi/\Phi_0\right)\right|$, where Φ_0 is the flux quantum $h/2e$. However, the *gate* tunable transmon we employ does not have such a straightforward relation to calculate its E_J. We can still describe the behavior of the qubit as a function of its characteristic parameters, namely the aforementioned E_J and the charging energy E_C, which is defined as

$$E_C = e^2/2C_\Sigma, \tag{2.55}$$

where $C_\Sigma = C_t + C_c + C_g$. First we will calculate the eigenenergies of the transmon, followed by taking a closer look at what makes a transmon a better qubit than the CPB. Lastly we will delve into how a qubit-resonator system interacts.

2.4.7.1.1 Transmon Hamiltonian

Crucial to the operation of a qubit are the anharmonicity and charge dispersion of the energy levels. In the ideal case, the anharmonicity is high in order to prevent the qubit from easily accessing higher modes than the two-level system it is intended to be. The charge dispersion is preferably as low as possible, because it describes the sensitivity of the qubit to any charges interacting with it, resulting in a shift of the qubit frequency. Both of these qubit properties can be expressed by the ratio of its Josephson energy and charging energy, E_J/E_C, which lie in order of 10-100 in the transmon regime [29]. The system with all cross

capacitances can be reduced to an effective circuit, of which the Hamiltonian is [63]

$$\hat{H} = 4E_c \left(\hat{n} - n_g\right)^2 - E_J \cos\hat{\phi}. \tag{2.56}$$

The number operator $\hat{n} = -q/2e$ counts how many Cooper pairs have crossed the junction and $n_g = Q_r/2e + C_g V_{in}/2e$ is the 'correcting' term to remove any offset number of pairs that come into the system by any other means (e.g. unintentional coupling via electrodes). Furthermore, the dimensionless gauge invariant phase $\hat{\phi}$ has been introduced, which corresponds to the phase difference across the junction of the macroscopic Cooper pair wave functions. One can rewrite this equation in terms of Mathieu characteristic values (see Ref. [64]), but here we will use the numerical approximation. We can rewrite Eq. 2.56 in a diagonalized truncated charge basis as [65]

$$\hat{H} = 4E_C \sum_{j=-N}^{N} \left(j - n_g\right)^2 |j\rangle \langle j| - \frac{1}{2} E_J \sum_{j=-N}^{N-1} \left(|j+1\rangle \langle j| + |j\rangle \langle j+1|\right), \tag{2.57}$$

where $2N+1$ is the number of charge basis states, which usually can lie around 40-100. The charge dispersion shows a decrease in sensitivity for increasing E_J/E_C, see Fig. 2.7, where sensitivity is heavily suppressed in the transmon regime of $E_J/E_C = 50$ [66].

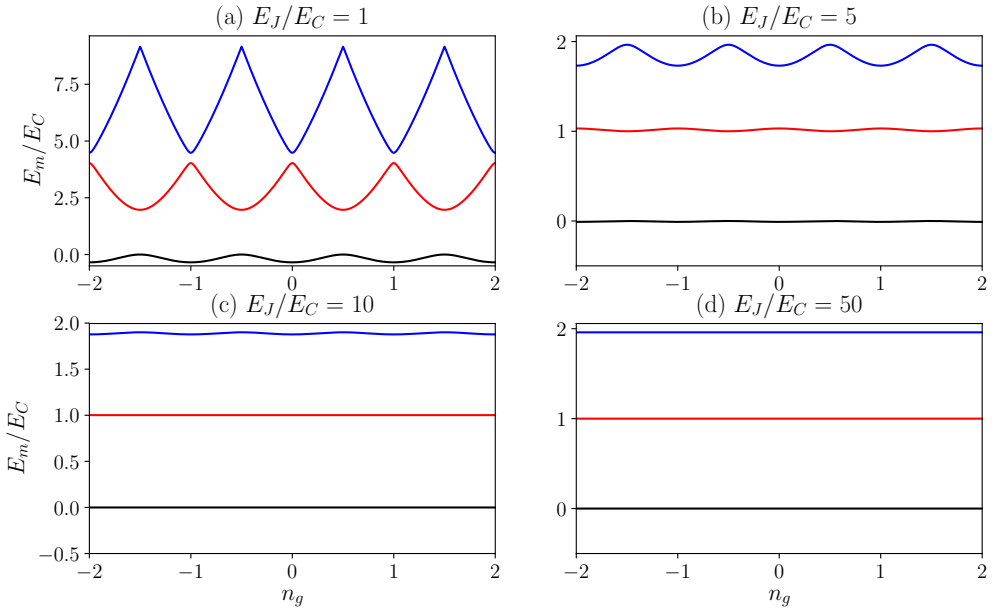

Figure 2.7: Eigenenergies E_m of the mth energy level for $m = 1, 2, 3$ in black, red and blue, respectively. For increasing E_J/E_C we see the charge dispersion be suppressed, up to a ratio of ∼50 which is the operation regime for a transmon. For this numerical simulation we have chosen $N = 100$.

The charge dispersion for the mth energy level, ϵ_m, is defined as the peak-to-peak energy range for varying n_g as

$$\epsilon_m = E_m\left(n_g = 1/2\right) - E_m\left(n_g = 0\right). \tag{2.58}$$

In the limit of small charge dispersion and large E_J/E_C the energy levels can be approximated by

$$E_m\left(n_g\right) \simeq E_m\left(n_g = 1/4\right) - \epsilon_m \cos\left(2\pi n_g\right). \tag{2.59}$$

An exact result of the charge dispersion is given by the limit of the analytical solutions of Eq. 2.56 for large E_J and results in [29]

$$\epsilon_m \simeq (-1)^m E_C \frac{2^{4m+5}}{m!} \sqrt{2/\pi} \left(E_J/2E_C\right)^{2m+3/4} e^{-\sqrt{8E_J/E_C}}, \tag{2.60}$$

for $E_J/E_C \gg 1$. The interesting part of this equation is the exponential decrease with $\sqrt{E_J/E_C}$, which proves that it is preferable to have as large a E_J/E_C as possible (limited by the needed anharmonicity).

2.4.7.1.2 Anharmonicity

To prove the anharmonicity for the transmon E_J/E_C regime, we can calculate the energy of the mth level by expanding the cosine in Eq. 2.56 around $\psi = 0$ to the fourth order and subsequently perform perturbation theory on the quartic term to obtain [29]

$$E_m \simeq -E_J + \sqrt{8E_J E_C}\,(m + 1/2) - \frac{E_C}{12}\left(6m^2 + 6m + 3\right). \tag{2.61}$$

Defining the absolute and relative anharmonicity as

$$\alpha \equiv E_{12} - E_{01}, \qquad \alpha_r \equiv \alpha/E_{01}, \tag{2.62}$$

with $E_{mn} = E_n - E_m$. Using Eq. 2.61 we can conclude that [29, 65]

$$\alpha \simeq -E_C, \qquad \alpha_r \simeq -\left(8E_J/E_C\right)^{-1/2}. \tag{2.63}$$

This shows that the anharmonicity decreases algebraically for increasing E_J/E_C. The transmon *exploits* this very fact because it is possible to change the E_J/E_C ratio by changing the capacitance of the transmon itself, thus being able to reach the regime where the charge dispersion is suppressed heavily while the anharmonicity is not hurt.

2.4.7.2 Transmon resonator coupling

When we let the transmon capacitively couple to the CPW resonator, we can describe the effective Hamiltonian in the limit of large resonator capacitance $C_r \gg C_\Sigma$ as [29]

$$\hat{H} = 4E_C\left(\hat{n} - n_g\right)^2 - E_J\cos\hat{\phi} + \hbar\omega_r\hat{a}^\dagger\hat{a} + 2\beta e V^0_{rms}\hat{n}\left(\hat{a} + \hat{a}^\dagger\right). \tag{2.64}$$

The resonator frequency is $\omega_r = 1/\sqrt{L_r C_r}$ and $\hat{a}\left(\hat{a}^\dagger\right)$ the annihilation (creation) operator of a photon. The ratio of gate capacitance and total capacitance is incorporated by $\beta = C_g/C_\Sigma$ and the V_{rms} of the oscillation between qubit and resonator is denoted by $V^0_{rms} = \sqrt{\hbar\omega_r/2C_r}$. Since we are mostly interested in the interaction between the first two qubit states, it is useful to rewrite this Hamiltonian in terms of transmon states $|i\rangle$ to obtain the generalized Jaynes-Cummings Hamiltonian [29, 67]

$$\hat{H} = \hbar\sum_j \omega_j\,|j\rangle\langle j| + \hbar\omega_r\hat{a}^\dagger\hat{a} + \hbar\sum_{i,j} g_{ij}\,|i\rangle\langle j|\left(\hat{a} + \hat{a}^\dagger\right). \tag{2.65}$$

This is the first time we encounter the (Hermitian) coupling term g_{ij}, here defined as

$$\hbar g_{ij} = 2\beta e V^0_{rms}\,\langle i|\,\hat{n}\,|j\rangle. \tag{2.66}$$

To simplify the Hamiltonian even more, we can look at the specific case the transmon operates as a two-level system, and we can define the ground-first level transition frequency as the *qubit* frequency $\omega_q = \omega_{01}$ and coupling $g = g_{01}$, using the same notation for transition differences as for energy levels $\omega_{ij} = \omega_j - \omega_i$. Furthermore, we make the assumption that $\omega_q \sim \omega_r$ and $\omega_r \gg g$, which allows us to use the rotating wave approximation to obtain

$$\hat{H} = \hbar\omega_r\hat{a}^\dagger\hat{a} + \hbar\omega_q\sigma_z/2 + g\left(\hat{a}\sigma_+ + \hat{a}^\dagger\sigma_-\right). \tag{2.67}$$

The last term shows the interaction term between the resonator and qubit, with an alternating exchange of a photon being absorbed and emitted by the qubit and resonator with rate g.

2.4.7.3 Measurement of characteristic features

As mentioned before, cQED operates in the strong dispersive regime [62]. In this regime, the detuning $\Delta_m = \omega_{m,m+1} - \omega_r$ between the mth qubit level and resonator frequency is large, which means $g/|\Delta| \ll 1$ and $g/|\Delta + \alpha| \ll 1$. Subsequently we can regard only the lowest order of qubit-resonator interaction by canonical transformation of Eq. 2.65 [29]. We should still allow virtual transitions to higher excited states because of the weak anharmonicity of the transmon and then we can apply the transformation and obtain

$$\hat{H}_{\text{eff}} = \frac{1}{2}\hbar\omega_q\sigma_z + (\hbar\omega_r + \hbar\chi\sigma_z)\, a^\dagger a \tag{2.68}$$

Where χ is the dispersive shift, defined as

$$\chi = \alpha\frac{g^2}{\Delta^2}. \tag{2.69}$$

This analytical result shows that ω_r is shifted when the qubit changes in state. Furthermore, the resonator and qubit both obtain a frequency shift when they come close together and form an avoided crossing. This level repulsion is characterized by

$$\delta = \frac{g^2}{\Delta}. \tag{2.70}$$

2.4.7.4 Sources relaxation time T_1

Unfortunately the qubit suffers from relaxation in energy, which is characterized by its relaxation time T_1. Several sources of decoherence are known and discussed below.

2.4.7.4.1 Spontaneous emission

Because the transmon is coupled to a transmission line, there is a possibility of energy leaking to that channel due to radiative decay. This can be approximated by regarding the traveling Cooper pairs as a classical dipole with length L, oscillating at a frequency ω_q to get the average power

$$P = \frac{d^2\omega_q^4}{4\pi\epsilon_0 3c^3}. \tag{2.71}$$

The dipole moment $d = 2eL$ can be calculated using an $L \simeq 15\,\mu\text{m}$, as estimated by Ref. [62]. Thus, the decay time of the first to ground level due to spontaneous emission is given by

$$T_1 = \hbar\omega_q/P = \frac{12\pi\epsilon_0\hbar c^3}{d^2\omega_q^3}. \tag{2.72}$$

In the range of our qubit frequencies, 3 to 8 GHz, the relaxation times are around 6 to 0.3 ms, respectively, and are therefore not a limiting factor in T_1 time.

2.4.7.4.2 Purcell effect

The spontaneous emission is amplified when coupled to a resonator, called the Purcell effect [68]. In the situation where all except the fundamental mode of the resonator are far detuned from ω_q, we disregard all the higher modes of the resonator. Using a single-mode approximation, the Purcell rate for decay is given by

$$\gamma_\kappa = \kappa\frac{g^2}{\delta^2}, \tag{2.73}$$

where $1/\kappa$ is the resonator lifetime. For a typical resonator of $Q \sim 10^4$ and a coupling detuning range of 1 GHz, the T_1 contribution is $\sim 200\,\mu\text{s}$. This value increases linearly with increasing resonator quality factor, it is therefore not unimportant that these resonators are of moderate quality as well.

2.4.7.4.3 Dielectric losses

There are several dielectrics present in the system, the substrates (either sapphire or crystalline Si), the MoRe-hBN interface between the superconducting islands of the transmon and the gate dielectric on top of the graphene.

The substrates are known to be very low in loss at cryogenic temperatures, $\tan\delta \sim 10^{-6}$ and 10^{-8} for Si and sapphire, respectively. However when using Si there is always the chance of dangling bonds due to oxidized amorphous SiO_2, which has a higher loss tangent of around 10^{-3}. There have been several efforts to reduce these dielectric losses [56], but for the application used in this research it unnecessary to optimize these interfaces, because they are not the limiting factor in T_1.

A possible loss channel is the interface between the graphene contacts through the hBN, however as of yet there has been no theoretical or experimental estimate of those losses.

The gate dielectric used in this thesis is SiN, which is known to be a lossy dielectric and expected to limit measurements of both T_1 and T_2, see Section 2.4.7.5.1.

2.4.7.4.4 Quasiparticle tunneling

There is always a possibility of quasiparticle tunneling through the JJ, due to accessible states in the superconducting condensate. In order to know this influence for graphene JJ, the hardness of the superconducting gap in the induced superconductive graphene should be known. As of writing this report, this is *not* known and therefore we are unable to approximate its influence on T_1. We do however postulate that a hard gap is crucial for a well working SNS transmon, both for T_1 and T_2.

2.4.7.4.5 Vortices

Vortices are created when a magnetic flux penetrates the superconductor. These vortices, once created, do not disappear until superconductivity is broken, because they are locally circulating currents without resistance. These vortices usually are pinned to defects in the superconducting film, but can move around and when they do, interact with the qubit and siphon energy from it. When using transmon qubits that are not magnetic field compatible, a lot of shielding is in place to decrease the magnetic field as much as possible. For a magnetic field compatible transmon different measures have to be taken to deal with vortices, which is discussed in Section 2.2.2.3.

2.4.7.5 Sources dephasing time T_2

2.4.7.5.1 Charge noise

The gate dielectric on top of the graphene will be the largest source of charge noise, due to possible defects in the dielectric. Since the electric field of the gate tunes the E_J by changing the available charge carriers in the graphene, any change in this field changes the E_J and thus the ω_q. SiN has been used as gate dielectric, which is known to have many of these defects. It is of interest to change and/or remove this dielectric in order to determine its influence on the qubit's dephasing time, for example with the much cleaner hBN.

2.4.7.5.2 Capacitive coupling gate leads

The E_J is tuned with gate leads, but these are closely placed to the JJ itself, and thus are prone to capacitive coupling with the SC. Especially at the gate where the supercurrent is highest in density, the influence of capacitive coupling might be a limiting factor in T_1. Simulations have been performed in order to estimate the capacitive coupling and will be investigated if these are limiting.

2.4.8 Graphene

Since its (re)discovery by Andre Geim and Konstantin Novoselov in 2004 [69], graphene has been used successfully in many different applications due to its interesting properties of conduction and strength. With this research we contribute to the vast amount of active topics involving graphene. There are several reasons for using graphene-superconductor devices, but it has only recently come to the point that graphene is useful in a high quality Josephson junction [31].

Graphene has a relatively high mobility and has ballistic transport for sizes used in these devices ($\sim$400 nm). For use as a Josephson junction, coherent transport between the superconducting leads is necessary, which is guaranteed by the ballistic transport of graphene. Calado et al. have shown ballistic transport with well-defined and transparent interfaces between graphene and its connected SC by encapsulating the graphene in hexagonal boron nitride(hBN) and contacting with MoRe [31]. The addition of hBN ensures that the graphene is actually atomically *flat*, as it is a crystalline structure, in contrast to depositing graphene on etched surfaces that come with a certain roughness.

Furthermore, since the aim is to build a magnetic field insensitive qubit, the superconductivity of the junction should not break down at high magnetic field. The single layer graphene is by definition one atom thin, and with the graphene being in an induced superconducting state, it is energetically favorable for the magnetic field to bend around the graphene. This makes sure that the supercurrent is unaffected by the magnetic field. Additionally, the current carrier density can be altered by applying an electric field, allowing the Josephson energy to be changed as a function of gate voltage. The dispersion diagram of graphene is schematically drawn in Fig. 2.8, showing that we can linearly adjust the carrier density of either the holes or electrons.

Moreover, the zero-electric field Josephson energy can supposedly reliably be targeted, as experience has taught that same graphene stack geometries result in reproducible critical currents. An additional feat that makes graphene easy to work with is its electrical sturdiness, in contrast to the highly ESD sensitive nanowires.

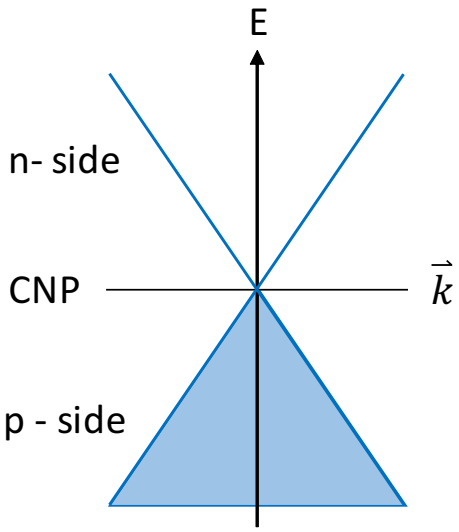

Figure 2.8: Linear band dispersion of graphene, shown here with zero carrier density at the charge neutrality point (CNP). The current carrier density can be changed to more holes on the p-side or more electrons on the n-side.

Chapter 3

Experimental setups

3.1 Magnetic field insensitive resonators

3.1.1 Device fabrication

Superconducting CPW resonators were fabricated from NbTiN films sputtered from a 99.99% purity NbTi target in an Ar/N atmosphere onto 2 inch 430 µm thick sapphire (0001) orientation wafers. A typical 100 nm film showed a T_c of 14 K, a resistivity of 123 $\mu\Omega\,cm^{-1}$ and exhibited compressive stress of −400 MPa. The resonators were defined using electron beam lithography and a subsequent reactive ion etch in an SF_6/O_2 atmosphere. A schematic fabrication scheme is shown in Fig. 3.3(a-c). The CPW resonators have a wavelength of $\lambda/4$, as they are shorted on one end to ground, whilst being open and capacitively coupled to a common feedline on the other end, as seen in Fig. 3.1(b). The CPW resonators measured for this thesis have been patterned with circular holes in a hexagonal lattice as artificial vortex pinning sites in and close to its center strip, see Fig. 3.1(c). The hole size is kept a constant 100 nm in diameter, the hexagonal lattice is changed in unit cell size per resonator to obtain a varying hole density between 0 and 28.8 μm^{-2}. The remainder of the ground plane is patterned with square holes in a square lattice.

3.1.2 Measurement setup

The device is placed in a light tight copper box and thermally anchored to a dilution refrigerator with a base temperature of 15 mK. To obtain information about the performance of the resonators in a magnetic field, the complex microwave transmission S_{21} through the feedline of the sample is measured using heterodyne demodulation technique, see Fig. 3.1. Systems where these resonators potentially could be used require single-photon level occupation of the cavities, thus the sample input line is strongly attenuated at the various temperature stages of the refrigerator, followed by amplification in the output line. An external magnetic field can be applied using a 3-axis 6-1-1 T vector magnet, in this case perpendicular to the surface of the sample.

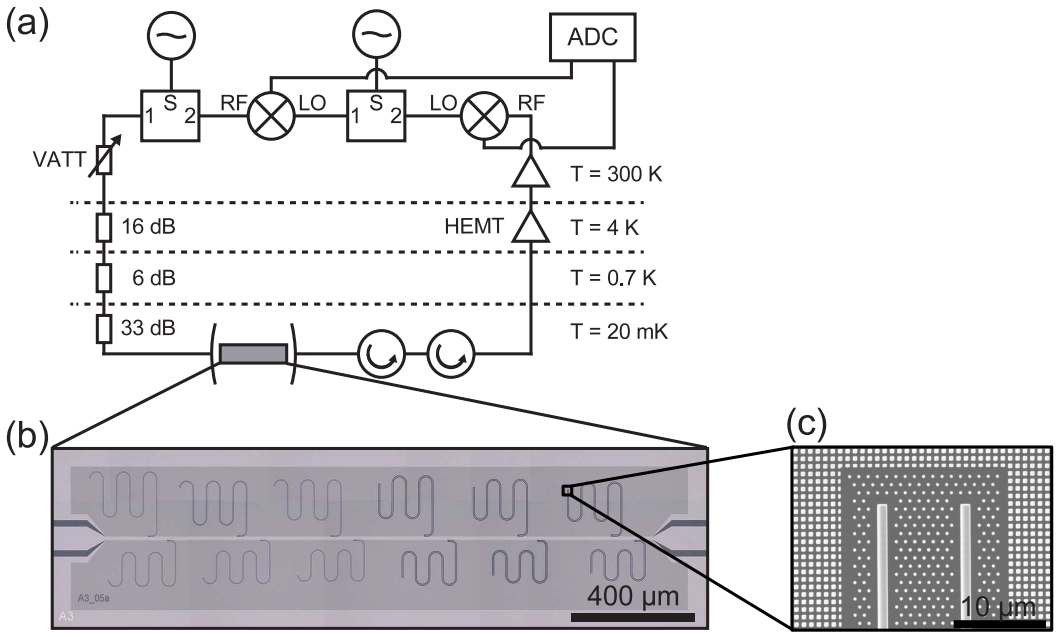

Figure 3.1: (a) Circuit diagram of the heterodyne measurement scheme. The RF readout signal is split, with one arm remaining at room temperature and the other passing through the sample. Both are downconverted to recover the amplitude and phase of the complex transmission S_{21}. (b) Optical image of the device where we see multiple resonators (with varying hole densities) frequency multiplexed to a common feedline. (c) Zoom in SEM image of the hexagonally antidot patterned resonator and the square patterned ground plane.

3.2 Transmon measurements

3.2.1 Graphene qubit

The device is placed in a light tight copper box and thermally anchored to a dilution refrigerator with a base temperature of 15 mK. During cooldown zero magnetic field is applied to the sample. To obtain information about the performance of the resonators and qubit in a magnetic field, the complex microwave transmission S_{21} through the feedline of the sample is measured using standard heterodyne demodulation techniques, see Fig. 3.2. To be used as qubit, the system requires single-photon level occupation of the cavity, thus the sample input line is strongly attenuated at the various temperature stages of the refrigerator, followed by amplification in the output line. An external magnetic field can be applied using a 3-axis 6-1-1 T vector magnet, in this case it is changed with 0.1 T steps from 0 to $B_{||}$ =1 T, meaning parallel to both the surface of the sample and the contacts of the graphene junctions, see Fig. 3.2(d). The constraint on the in-plane magnetic field is set firstly by the sensitivity of the patterned CPW resonators to perpendicular magnetic field. Secondly, it is set by possible flux-focusing effects at the contact leads, which could lead to magnetic field penetration of the junction. This would locally destroy the induced superconductivity and decrease the supercurrent.

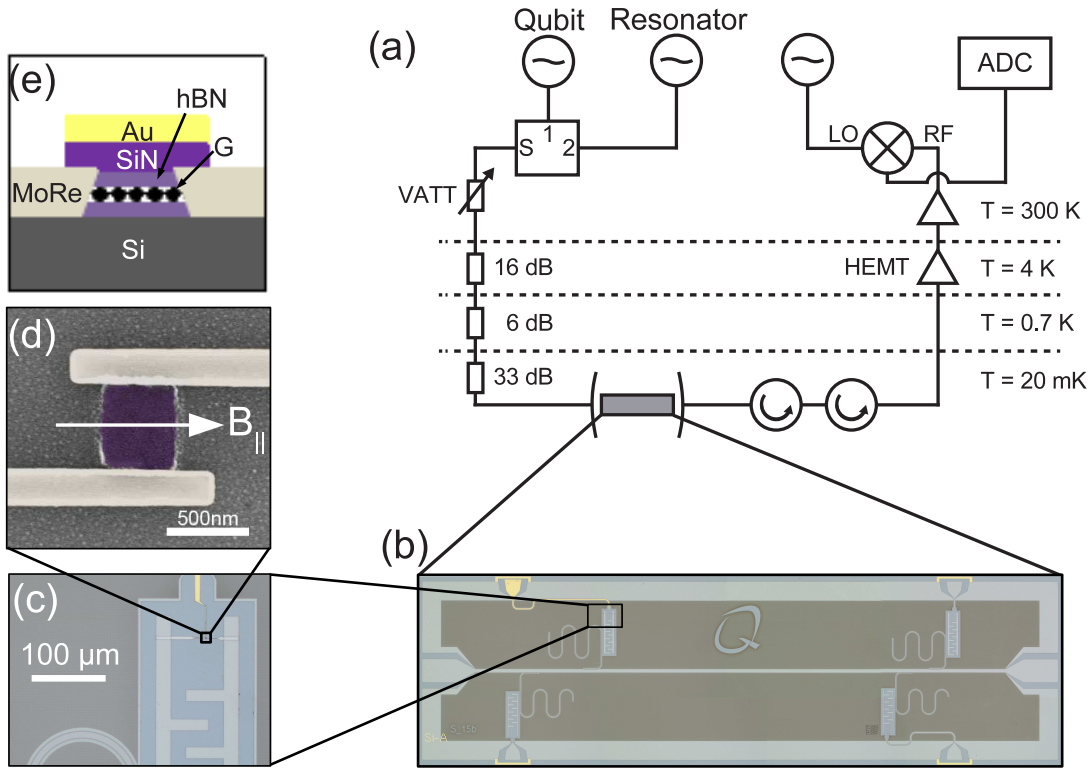

Figure 3.2: (a) Circuit diagram of the heterodyne measurement scheme with resonator and qubit RF sources. This setup is used both for measurement of the graphene qubit as well as the Al/AlOx transmon. (b) Optical image of the device with resonators frequency multiplexed to a common feedline. (c) Zoom in optical image of the transmon and its graphene Josephson junction with gold gate on top. (d) False colored SEM image of the junction consisting of single layer graphene sandwiched in the direction perpendicular to the page with hBN and contacted with two narrow leads of MoRe. The magnetic field is applied in the direction of the arrow. (e) Schematic drawing of a cross-section of the Josephson junction. The single layer graphene is sandwiched with two hBN flakes, contacted to MoRe leads, after which the dielectric SiN and gold gate is sputtered.

3.2.2 Al/AlOx transmon

The measurement setup of this sample is identical to the graphene qubit, with the exception of removing all possible magnetic field from the sample. That means mounting the sample in a light tight aluminium box with additional Eccosorb taped around, wrapped in NbTiN film. To remove any stray magnetic fields from the vector magnet, the magnet leads are shorted in this experiment.

3.2.3 Measurement techniques

Transmon measurements have been performed in two domains, continuous wave (CW) and time domain (TD).

3.2.3.1 Continuous wave

Continuous wave measurements have readout and drive sources constantly turned on, i.e. the sample is always irradiated with a readout (and qubit drive when applicable) signal. This has the advantage that we

can start and stop the acquisition of S_{21} at any time, as there is always a signal coming out of the output. This advantage also means that we can perform more measurements per timescale, as we do not have to time our input/output signal and wait for the system to relax to the ground state. The downside is that qubit measurements of T_1 and T_2^* are not possible, as the continuous drive does not allow the qubit to decay.

3.2.3.2 Time domain

Timing becomes important when probing the sample with measurements in the time domain. In this situation, timing of input signals and output acquisition is of utmost importance. The qubit is excited with a Gaussian π-pulse and depending on the type of measurement one wants to take, a readout pulse follows after a certain period of time, after which acquisition of that pulse is timed to be exactly when the microwaves have traversed the entirety of the cable length from start to finish.

3.3 Devices fabrication

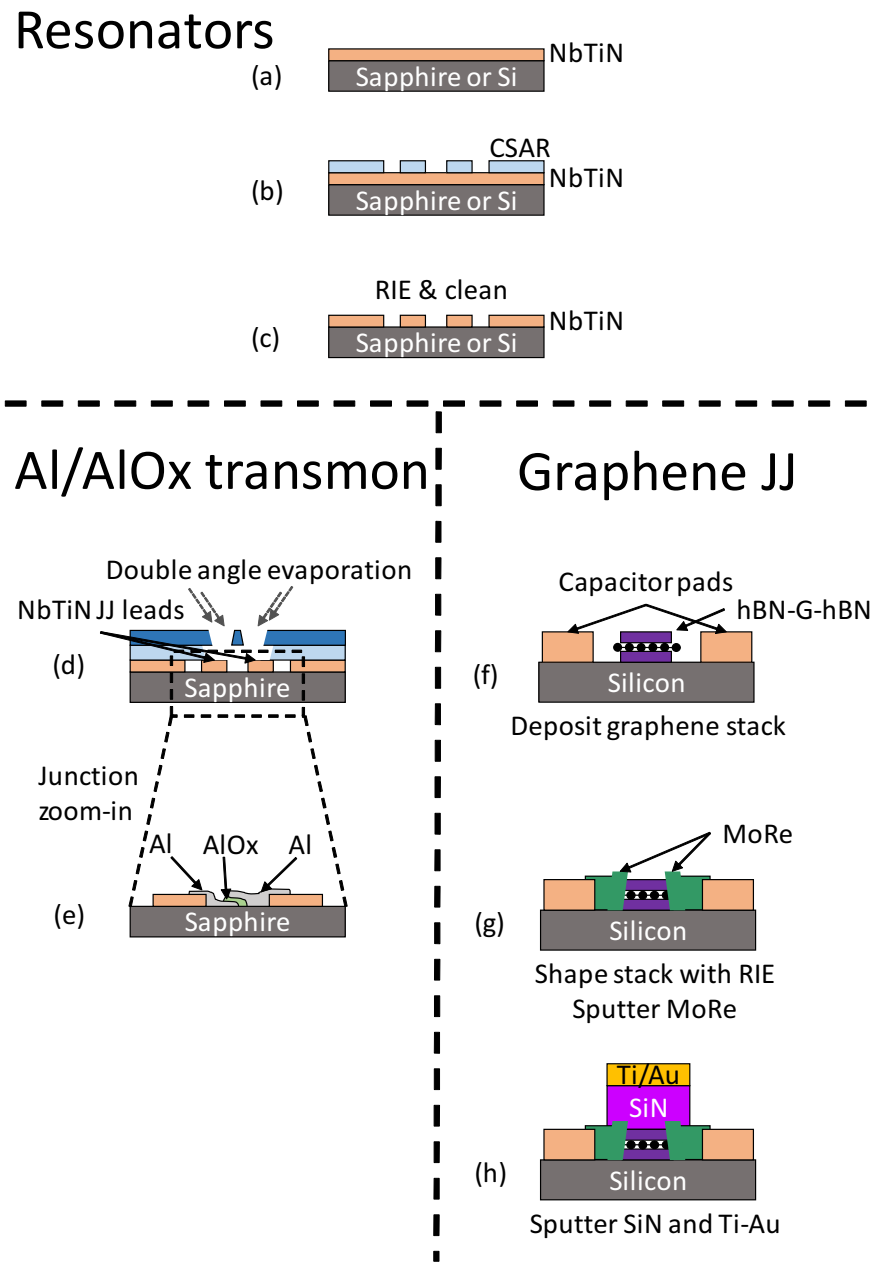

Figure 3.3: All devices discussed in this thesis have a superconducting NbTiN ground plane and patterned resonators. (a) Either a sapphire or silicon substrate is used on which a thin-film (20 nm) NbTiN layer is sputtered. (b) The resist is patterned by an e-beam lithography (c) The resonator (and their artificial pinning sites if applicable) pattern is etched in the NbTiN by using reactive ion etching (RIE) and resist is cleaned off the surface. (d) For the Al/AlOx transmon we continue with the sample as is in (c) and double resist layer is deposited and patterned to bare the substrates for deposition of the leads to the Josephson junction. The SIS junction is created by double angle evaporation, leading to (e) where a close-up of the Al/AlOx/Al junction is shown. (f) For the graphene junction, we deposit the hBN-G-hBN stack in between the transmon capacitor plates of the sample etched in (c). (g) The stack is contacted by an etch-fill, filled with sputtered MoRe, connecting the junction to the NbTiN plates. To reduce the amount of dielectric, the stack is shaped to a size of 500x500 nm. (h) The junction is top gated with 120 nm of sputtered SiN, followed by 100 nm of evaporated Au with 10 nm Ti sticking layer.

3.3.1 Simulations

All FEM simulations have been performed using CST Studio Suite®. Since we want to determine the E_C of qubit geometry in general (in this case of a transmon), we have to calculate the capacitances between the qubit and the systems it is coupled to (Eq. 2.55). These can be implemented with different levels of complexity, starting from the simplest case of having the largest capacitor plates and the ground solely, to the most complex system of adding full resonators and gate leads. A schematic of different capacitances for the most complex system is shown in Fig. 3.5. This is modeled with a 20 nm thin film of PEC (Perfect Electrical Conductor) and 40 µm of either silicon or sapphire substrate, using a cryogenic dielectric constant of 11.45 and 10.35, respectively.

3.3.1.1 Calculating capacitance

There are two ways of calculating the capacitance of the total network. The **RF-domain frequency solver** allows us to probe the capacitance at a certain location, where the solver probes capacitances it senses from each defined island. In our case we pick the approximate location of the Josephson junction, as this is where the E_J and E_C 'interact'. This is the quickest way of probing the capacitance, since it immediately outputs C_Σ.

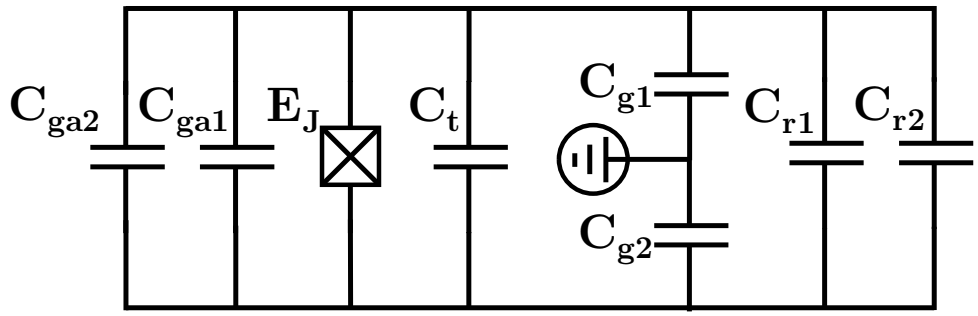

Figure 3.4: Schematic diagram for calculating C_Σ. The evaluation point of C_Σ is the Josephson junction.

The second solver is the **E-static solver**, which calculates capacitances between island from potentials applied to them. Since capacitance does not depend on potential difference between two charge carrying conductors, this can be any potential, as long as all potentials between all islands are different. With potentials defined in Fig. 3.6, we can calculate E_C via Eq. 2.55, but with C_Σ comprised of the full capacitance network, drawn in Fig. 3.4 and C_Σ defined as

$$C_\Sigma = C_{ga1} + C_{ga2} + C_t + \frac{C_{g1}C_{g2}}{C_{g1} + C_{g2}} + C_{r1} + C_{r2}. \tag{3.1}$$

The same type of summation of capacitances can be done when simulating different configurations of capacitance islands, e.g. removing the gate leads, and the equations are altered accordingly. Both solver methods have been used to confirm their validity and reliability.

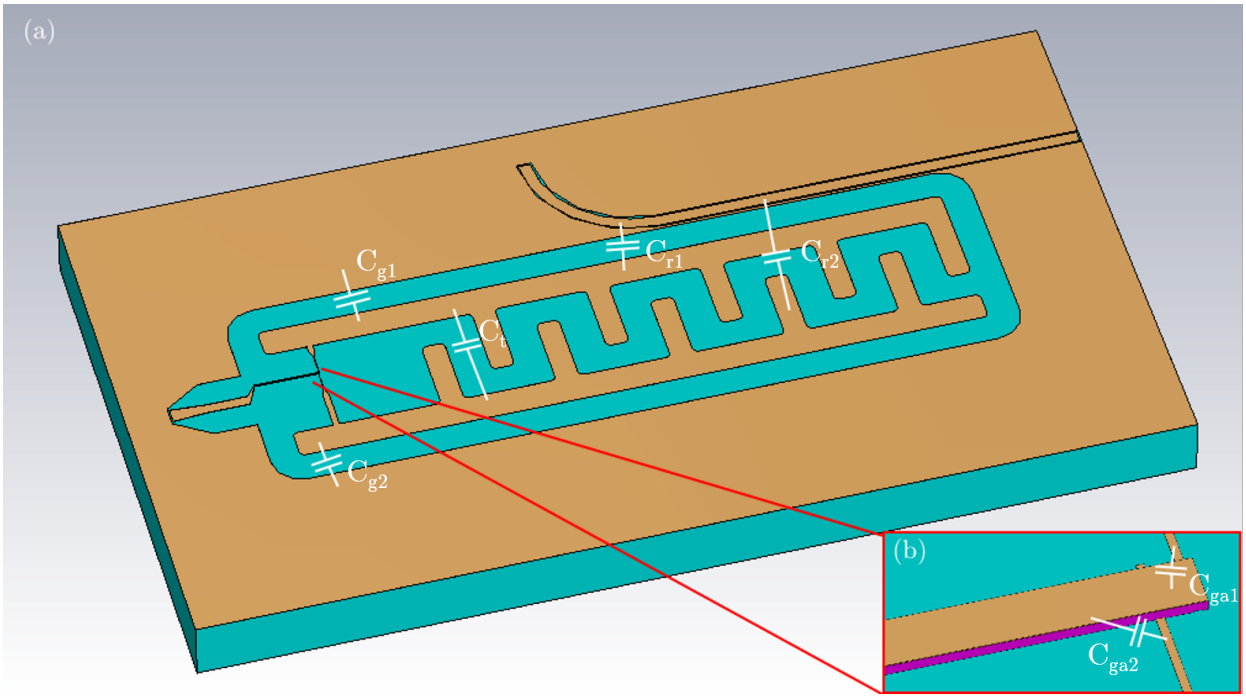

Figure 3.5: (a) 3D model used in calculations for a graphene transmon and schematic representation of the capacitances as defined in the circuit diagram of Fig. 3.4. (b) Zoom in of the Josephson junction and gate with SiN dielectric (purple) on top of the superconducting MoRe leads. The circuit equivalent capacitance to the gate is also added schematically. All superconducting films have been modeled as perfect electrical conductor (PEC).

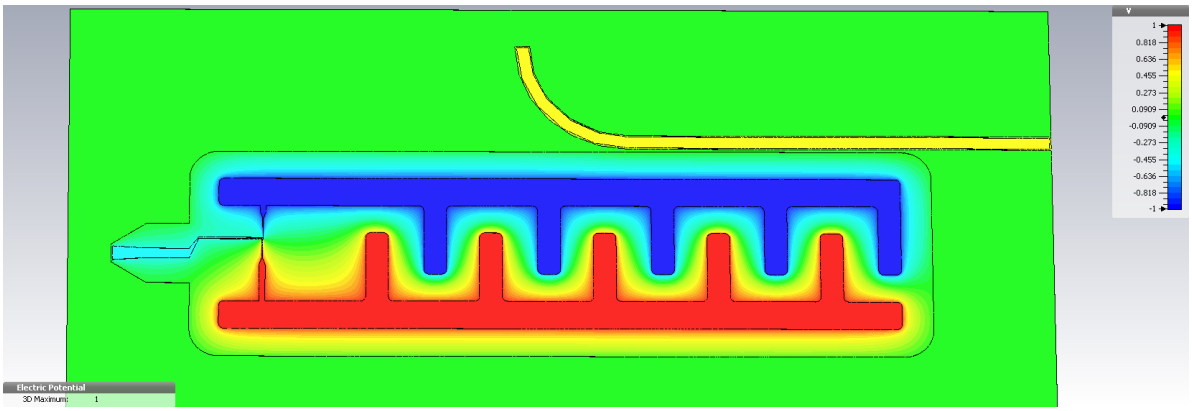

Figure 3.6: Defined potentials for a 3D model. Different colors are different potential values.

Chapter 4

Results and discussions

4.1 Magnetic field insensitive resonators

We start with investigating the first ingredient of a field insensitive qubit, the resonator. As explained in previous chapters, resonators patterned with artificial pinning sites have been shown to exhibit insensitivity to applied parallel magnetic field in Q_i and a parabolic relation in terms of resonance frequency. Vortices nucleate perpendicular to the sample's surface, due to a parasitic perpendicular component in parallel applied magnetic field from misalignment. These vortices will get trapped in the pinning sites up to the saturation of all holes. To confirm this assumption, we want to find the threshold value of the applied $B_\perp$ where all holes in the resonator are filled with vortices, and track the resonance performance until that point is reached. When all holes are filled, vortices nucleate outside of the artificial pinning sites and will move around, reducing the Q_i of the resonator by orders of magnitude. At the same time, the more untrapped vortices there are, the more normal metal is within the superconductor. Consequently, the f_r is reduced by the increased absence of Cooper pairs.

We extract each resonator's Q_i and f_r from the fit of Eq. 2.51 to the measurement of the feedline transmission S_{21} as function of input photon frequency at single-photon level power. We can subsequently apply this procedure for different $B_\perp$ and thus obtain Q_i and f_r as function of $B_\perp$. We perform this procedure for all resonators on the chip, thus adding a dimension of ρ_{hole}. In Fig. 4.1 we show $|S_{21}|$ and its fit as function of the readout frequency for two resonators with $\rho_{hole} = 1.8$ and $28.9\,\mu\mathrm{m}^{-2}$, at $B_\perp = 0\,\mathrm{mT}$ and the highest $B_\perp$ value for which a reliable fit was still possible. The total set of Q_i's and f_r as function of $B_\perp$ and hole density is shown in Fig. 4.2.

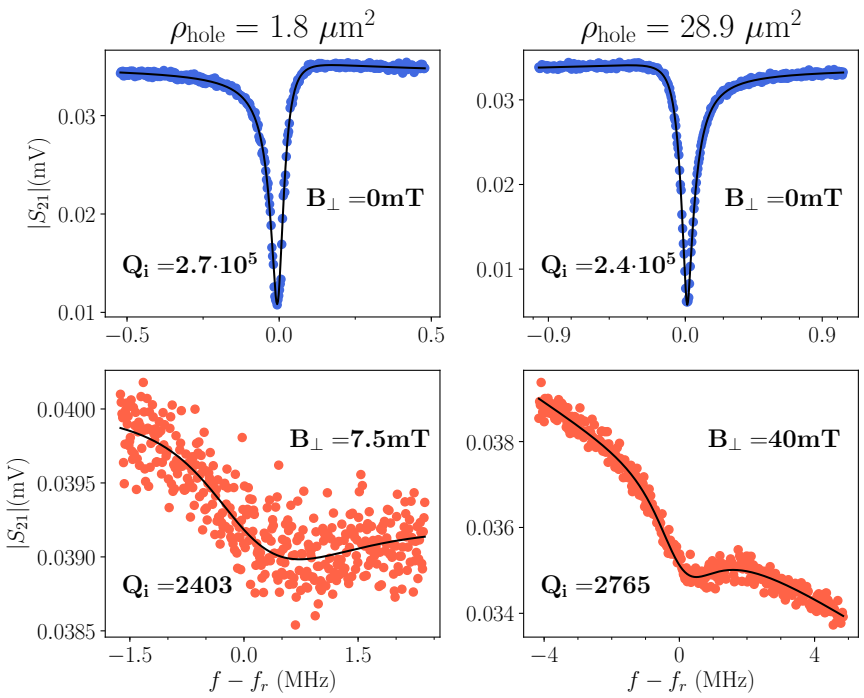

Figure 4.1: Relative Qi vs power for different magnetic fields (colourbar)

It is important to note that the magnetic field is applied in a 'field cooled' fashion, the sample is brought at $T > T_c = 15\,\text{K}$ whilst the magnet is still superconducting and set to a specific field value, after which the sample is cooled to base fridge temperature. All resonator S_{21} are then measured and the procedure is restarted. As this requires delicate fridge control, the procedure is performed manually and is therefore time consuming, which explains why the $B_\perp$ resolution is not as small as one would choose it to be for an programmed measurement.

The reason for such a complex procedure stems from earlier measurements where $B_\perp$ was changed with the sample at base temperature where, with using two different magnet power supplies, repeated resonance traces were not reliable enough to obtain steady and consistent Q_i measurements for the same resonator. This is indicative of vortices interacting with the resonator in an irregular way, such that extracting data from using this measurement technique became impossible. As these fluctuations were not observed when performing the field cooled measurement technique, it was decided to use that and accept less data points in exchange for higher quality data.

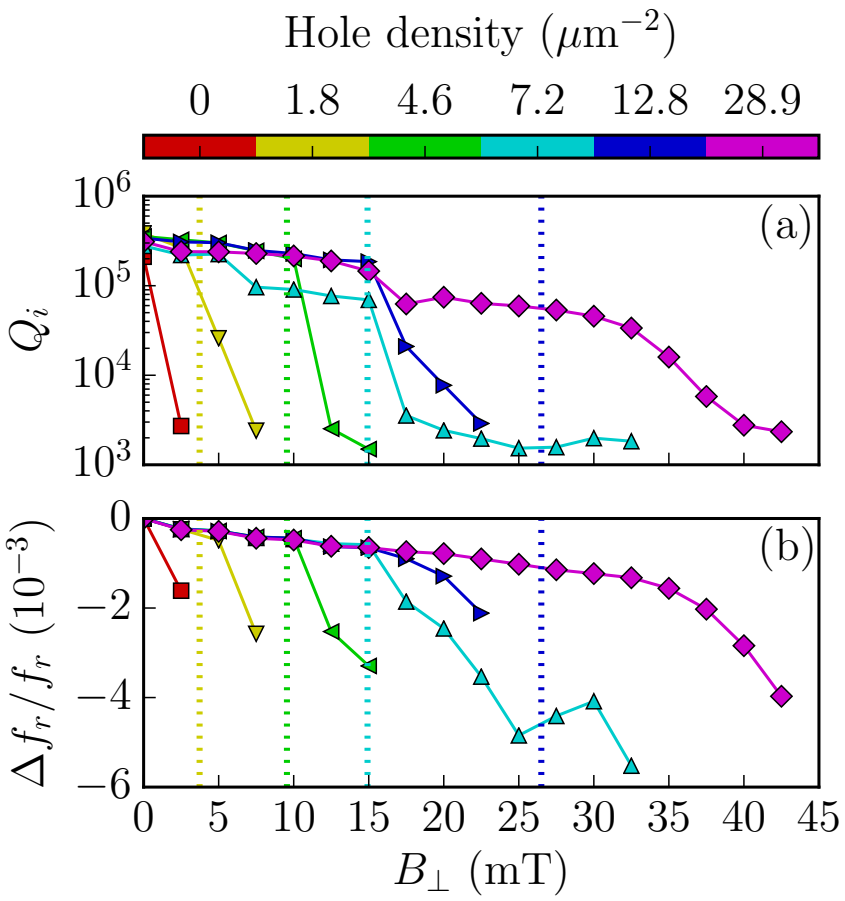

Figure 4.2: For each resonator (with different ρ_{hole}) the (a) Q_i and (b) $\Delta f_r/f_r$ at single photon level readout power was extracted from the feedline S_{21} and shown as function of $B_\perp$. Vertical dotted lines denote the calculated B_th, which are well in agreement with the abrupt decrease in both Q_i and f_r, indicating that at those $B_\perp$ values all pinning sites are filled and additional vortices exist more freely in the system.

Using the field cooled measurement technique we see a clear resonator performance increase for higher $B_\perp$ when the hole density is increased, as the Q_i remains around its zero field value for increasing magnetic field. The same trend is recognized in $\Delta f_r/f_r$. For different hole densities, the Q_i and f_r have an abrupt decrease for a subsequent $B_\perp$, which is the aforementioned threshold of filling up all holes in the resonator with vortices. We have estimated the threshold magnetic field B_th for the saturation of holes by vortices and shown as vertical dotted lines in Fig.4.2. This estimation is well in agreement with the observed abrupt decrease in either Q_i or $\Delta f_r/f_r$ up to a hole density of $7.2\,\mu\mathrm{m}^{-2}$.

4.1.1 Power and magnetic field dependent Q_i

We can show the existence of B_th, the saturating of the pinning sites, in an additional way. The Q_i for a resonator in zero magnetic field should increase for increasing power as surrounding TLSs will be saturated by the vast amount of energy being pumped in the system, allowing the resonance to become less spread in frequency (which has an increasing effect on Q_i) [56]. However, in a resonator system where free roaming vortices are present, increasing the power will decrease the Q_i [37]. Vortices are oscillating by effect of the readout microwave photons, which in turn increases the internal energy loss of the resonator, reducing Q_i. To visualize this we show the Q_i of each resonator at different readout powers, normalized to its Q_i at single-photon level, for every applied magnetic field and the different hole densities in Fig. 4.3.

We can clearly observe a 'fan' shaped pattern, from increasing (>1) to decreasing (<1) normalized Q_i for

increasing magnetic field at hole densities $\geq$7.2 µm^{-2}. For ρ_{hole} <7.2 µm^{-2} the fan shaped trend is less clear, with aberrations that do not coincide with the expected behavior of the normalized Q_i, with the exception of the resonator with $\rho_{hole} = 0$.

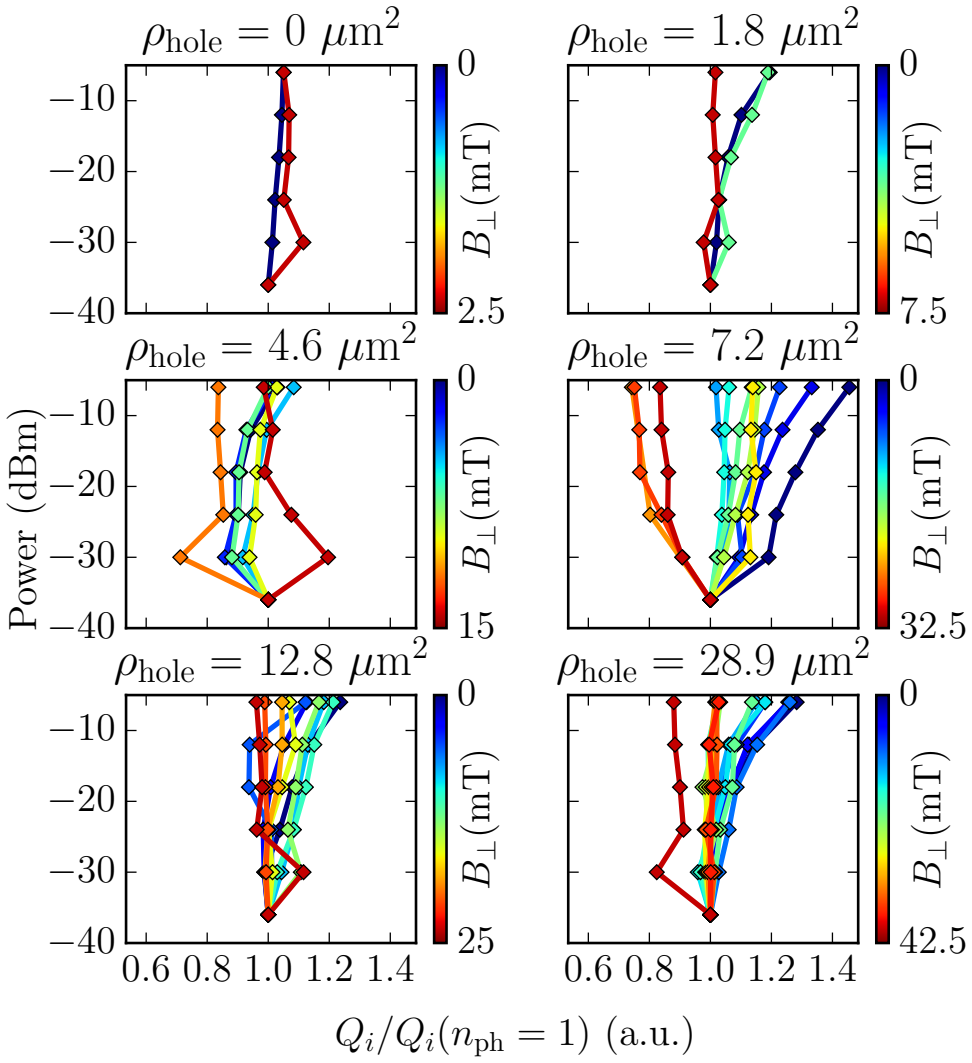

Figure 4.3: Readout powersweep of Q_i normalized to its single photon value for resonators with increasing hole densities, with individual lines signifying different $B_\perp$. We recognize a 'fan' shaped pattern of decreasing Q_i for increasing readout power when the $B_\perp$ is larger. This implies that vortices are moving freely at those $B_\perp$ values when $Q_i/Q_i(n_\mathrm{ph} = 1) < 1$ for higher readout power. The B_th for which this occurs is in line with Fig. 4.2 as the B_th is larger for increasing ρ_{hole}.

Not all resonators exhibit the 'fan' shaped pattern of lower normalized Q_i for higher readout power at (per resonator) maximum $B_\perp$. We see for several resonators that the (per resonator) maximum $B_\perp$ trace as function of readout power can be with normalized $Q_\mathrm{i} > 1$, instead of the expected $Q_i/Q_i(n_\mathrm{ph} = 1) < 1$. This can be explained by the uncertainty in the S_{21} fit using Eq. 2.51, which can misrepresent the ratio between Q_i at single photon level and higher readout powers.

4.2 Graphene transmon

In this section the results of the first working graphene transmon device in both zero magnetic field and at $B_{||} = 1\,\mathrm{T}$ is presented. We go through checks necessary in order to prove that a qubit is present, starting with characterizing the resonator coupled to the graphene transmon at high and single photon level readout power. To check that a resonance frequency level repulsion is caused by the transmon, we sweep the gate voltage to find an avoided crossing, tuning the qubit frequency through the single-photon resonator frequency. Finally, we perform qubit spectroscopy for different gate values. All these measurements were done with CW spectroscopy. Time domain pulsing has been attempted, but no qubit response has been detected. Every measurement type described above has been performed at both zero and $B_{||} = 1\,\mathrm{T}$ with qubit frequency tracking in between.

4.2.1 Zero magnetic field

We start investigating the device in its most basic configuration, setting $B_{||} = 0\,\mathrm{T}$ and characterize the resonator. When the superconducting magnet power source is turned on, but set to $B_{||} = 0\,\mathrm{T}$, the feedline transmission S_{21} measurement showed a very unstable resonance, as seen in Fig. 4.4(a). Averaging of each data point is being performed, which takes a finite amount of time. Fluctuating f_r at high frequency manifests itself exactly as Fig. 4.4(a), an average decrease of $|S_{21}|$ over a larger readout frequency range, with a superimposed staggered $|S_{21}|$ value due to the variation of f_r. In colloquial terms, the resonator is 'jumping around' in frequency space.

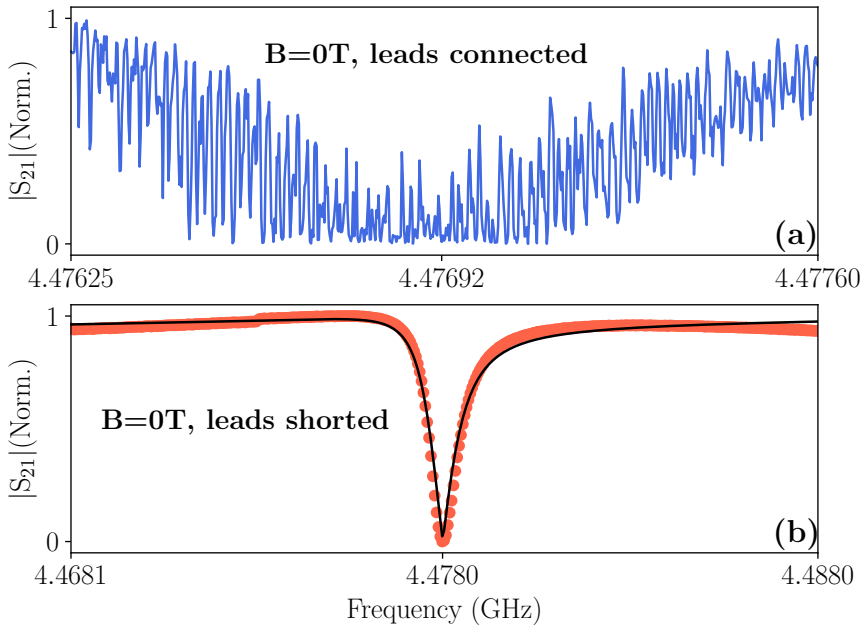

Figure 4.4: Normalized $|S_{21}|$ transmission measurements around the f_r of the resonator coupled to the qubit as function of readout frequency are shown both for $B = 0\,\mathrm{T}$, in one situation where the magnet leads are connected to the current supply (a) and when they are disconnected and shorted (b), with the fit of the measurement data to Eq. 2.51 as the solid black line. The f_r fluctuates when the leads are connected, making the measurement setup in this way unusable for qubit spectroscopy. The fluctuation vanishes when the magnet leads are shorted together, preventing any stray magnetic fields from the superconducting magnet to influence f_r. The $|S_{21}|$ measurements are performed at an input power larger than the single photon level.

It seems counterintuitive for a designed-to-be magnetic field insensitive resonator to have such an ill-defined resonance frequency at $B_{||} = 0\,\mathrm{T}$ with the magnet power supply leads connected. If stray fields do exist as result of fluctuations around the 'zero' current output of the source, surely the resonator should

be able to withstand sub-mT magnetic fields in all directions. We will see later that the resonator performance is increased at $B_{||} = 0\,\mathrm{T}$ only *after* the sample had been at 1 T, even with the lead connected (see Section 4.2.3.1).

With the magnetic field being the important factor of change, implied is a freezing out of otherwise freely interacting dipoles, or another form of stray TLS that can be directed with magnetic field. We can say with strong conviction that it was not vortices that were interacting with the resonator at the initial $B_{||} = 0\,\mathrm{T}$, as they would have been abundantly present after sweeping down from $B_{||} = 1\,\mathrm{T}$, but no such staggered $|S_{21}|$ has been seen again.

Since we require a well defined resonance frequency to be able to perform qubit spectroscopy, it was decided to remove the current source connected to the superconducting magnet completely and short the magnet leads to prevent any leftover fluctuating currents to create stray magnetic fields. In this configuration the resonance frequency is well defined and we can continue with S_{21} measurements. All subsequent zero magnetic field measurements were performed with the magnet leads shorted, unless stated otherwise.

4.2.1.1 Qubit resonator powersweep

We continue with investigating the resonator when using a lower readout power, to the point where we inject single photon microwaves into the feedline-resonator-qubit system. The normalized feedline transmission S_{21} of the sample as a function of readout frequency and readout power near $f_{r,\mathrm{bare}}$ (the resonance frequency for high input power) is shown in Fig. 4.5(a). From that powersweep we take two linecuts, one at a 'high' readout power, where n_{ph} is high enough in the resonator such that no level quantization occurs and a linecut at $n_{\mathrm{ph}} \approx 1$. The fit parameters extracted from the measurement data to Eq. 2.51 are presented in Table. 4.1. The change to $f_r < f_{r,\mathrm{bare}}$ shows us that at 0 T the resonator interacts with a two-level system, which prompts us to investigate whether or not this two-level is indeed the graphmon. The magnitude of the level repulsion $\delta \approx -3\,\mathrm{MHz}$ at a gate value of 167.4 mV.

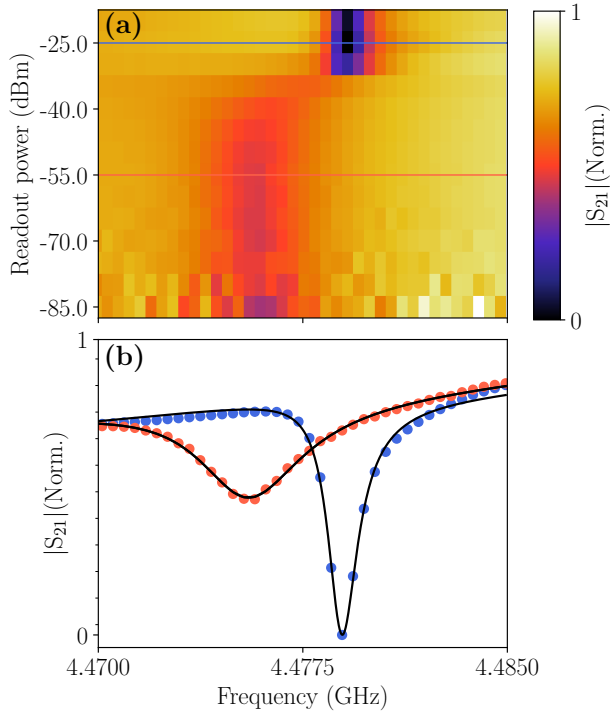

Figure 4.5: Readout powersweep of the resonator coupled to the graphmon at a gate value of 167.4 mV, which shows a level repulsion of $\delta \approx -3\,\mathrm{MHz}$, indicating that $f_q > f_r$. The minimum of the normalized $|S_{21}|$ increases when the resonator-qubit level repulsion occurs, which is an indication of an unstable f_q, a sign of low T_2.

Table 4.1: Fit parameters extracted from Eq. 2.51 at single-photon level and high readout power for resonator S_{21} traces shown in Fig. 4.5.

Fit parameter	$\mathbf{n_{ph}}$ **saturated**	$\mathbf{n_{ph} \approx 1}$
f_r	4.479 GHz	4.475 GHz
Q_l	3100	938
Q_i	4406	1070
Q_c	10455	7619
Q_e	10271	7508

4.2.1.2 Resonator spectroscopy with qubit gate sweep

We know from Section 2.4.7.2 that the level repulsion depends on f_q, where the closer f_q is to $f_{r,\mathrm{bare}}$, the larger δ becomes. We have a gate capacitively coupled to the Josephson junction which can change the amount of charge carriers in the graphene, therefore changing its E_J (as E_C is constant by geometrical constraint). We can change the DoS of the graphene from depleted (p-side) through the CNP to the electron filled level (n-side). Thus, changing the gate voltage will result in a response to the resonator, changing its f_r. The resonator spectroscopy as function of gate voltage is shown in Fig. 4.6. We observe the expected $f_q \gg f_{r,\mathrm{bare}}$ when many charge carriers are present and see several avoided crossing of the f_q moving from $f_q < f_r$ to $f_q > f_r$.

The fact that we see f_r change with V_gate is encouraging, it indicates that the two-level system that causes the level repulsion is the graphene qubit.

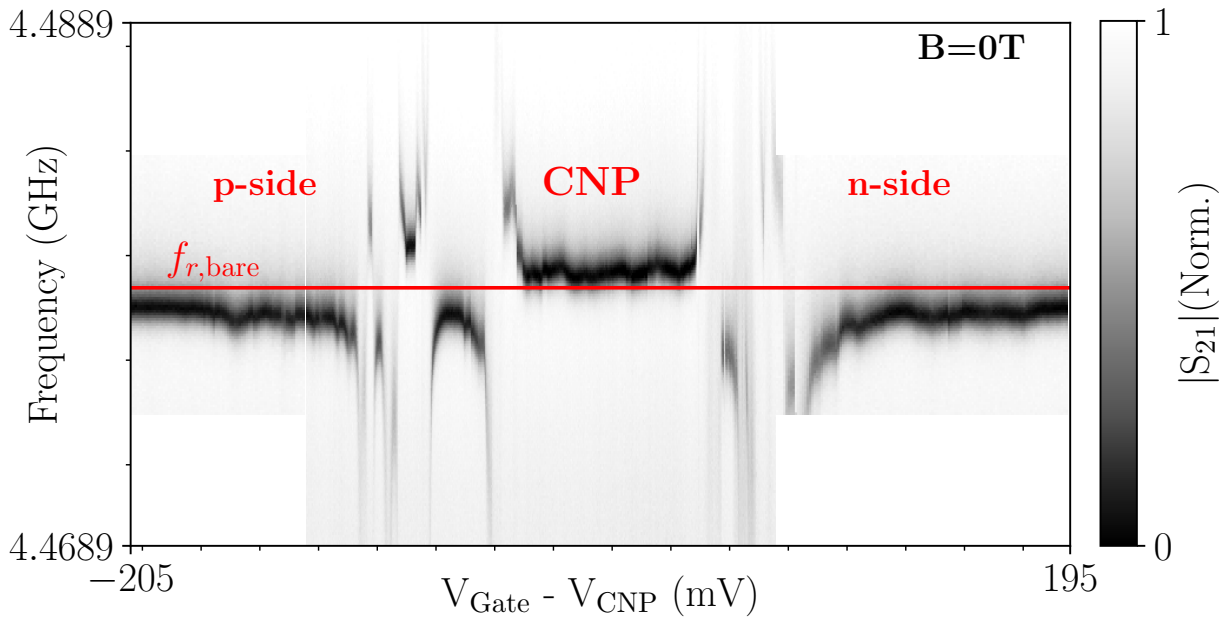

Figure 4.6: Normalized resonator transmission $|S_{21}|$ as function of readout frequency and applied gate voltage, centered around the CNP of the junction. We can see that the f_q indeed changes with changing gate voltage, moving through f_r many times from CNP to both n- and p-sides, creating several avoided crossings. A zoom-in of one avoided crossing is showed in Fig 4.7. $V_\mathrm{gate} - V_\mathrm{CNP}$ might differ in plots throughout this thesis due to gate voltage drift.

4.2.1.3 Avoided crossing

We will now zoom in on the f_q moving from $f_q < f_r$ to $f_q > f_r$, an avoided crossing from the resonator-gate sweep, as shown in Fig 4.7.

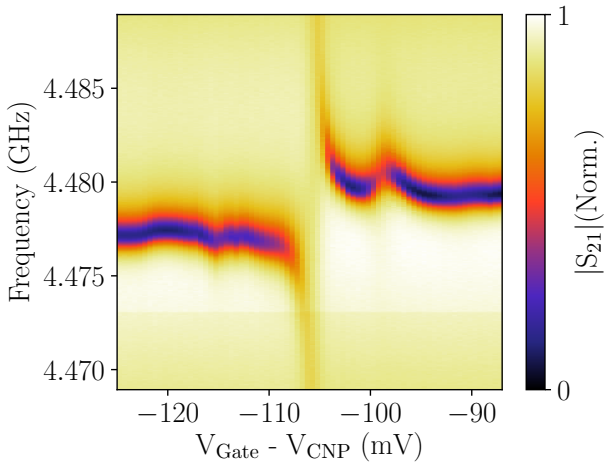

Figure 4.7: Zoom-in of an avoided crossing from Fig. 4.6. Besides the avoided crossing we observe a 'bump' at both -100 and −115 mV, where the qubit moves closer but does not cross $f_{r,\text{bare}}$.

The next step involves driving the qubit directly, sweeping the qubit drive whilst keeping the resonator readout tone constant, i.e. performing CW two-tone spectroscopy and observe a dispersive shift χ on top of the level repulsion δ. This proved to be unfeasible as no dispersive shift could be found for a range of qubit drive and resonator readout powers. However, since we do observe a qubit signature, it had been decided to increase the $B_{||}$ up to 1 T and perform the same type of analysis this chapter has shown.

4.2.2 Changing the magnetic field

Now that we have seen that there is a graphene qubit present at 0 T, we want to increase the $B_{||}$ up to the maximum value that the fridge magnet can attain, which is 1 T. Whilst going up in magnetic field along one axis, $B_{||}$, due to small errors in the alignment of the sample and magnet control, constant alignment of the field is necessary in order to be sure the field is parallel to the surface of the sample. Errors in alignment become significant enough to manually re-align every 0.1 T. An example of such an alignment procedure is shown in Fig. 4.8, where resonator spectroscopy is used as an alignment aid.

First, the field is increased to $B_{||,\text{old}} + 0.1$, in this procedure the f_r decreases as we have seen before for the resonators with holes in parallel magnetic field. However, every offset from perfect parallelity reduces f_r as more Cooper pairs are broken up in the superconductor. The field alignment is corrected by picking the magnetic field angle of the designed parallel axis such that f_r is at its maximum. It is important to note that the magnetic field angle sweep is hysteretic, as is the case with most magnetic field changes in combination with superconductors. This requires 'smart' sweeping, as overshooting the maximum f_r means the offset degree value of that maximum f_r will change when sweeping back. Furthermore, small degree steps are taken in order to keep the hysteresis to a minimum.

Further analysis of the magnetic field sweep data, e.g. level repulsion as function of field, can be found in Section 4.2.3.6.

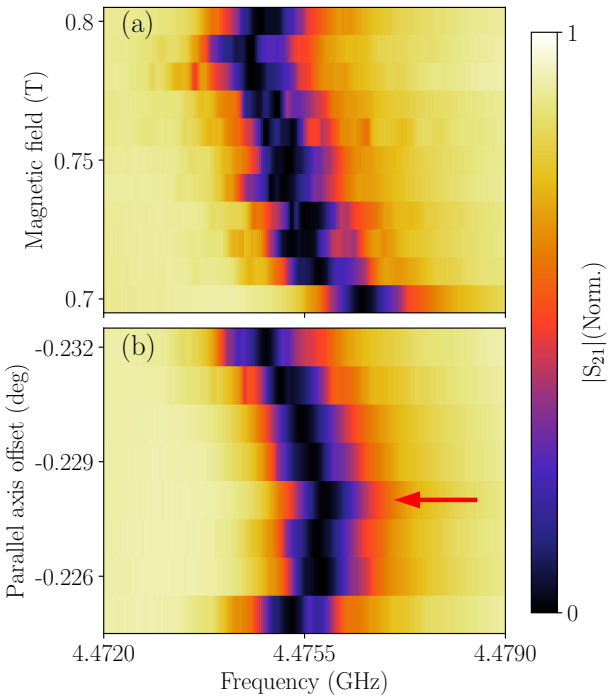

Figure 4.8: (a) An example of magnetic field increase from 0.7-0.8 T followed by (b) alignment of the parallel axis to find the largest f_r, and set the parallel axis offset to that value, in this case the value denoted by the arrow.

4.2.3 Finite magnetic field

At this point in the experiment we have successfully reached an aligned $B_{||} = 1\,\mathrm{T}$ and we will perform the same analyses on the resonator-qubit system to determine its usability and performance, now in a magnetic field.

4.2.3.1 Resonator powersweep

The powersweeps and linecuts at select readout powers of the resonator at 0 and 1 T are shown together in Fig. 4.9. This figure carries evidence that the antidot patterned resonator that is coupled to the qubit is, up to the measured 1 T, magnetic field insensitive. As can be seen from the hanger parameters (Eq. 2.51) extracted from the fits shown in Table 4.2, the f_r is reduced by 5 MHz at $B = 1\,\mathrm{T}$, which is expected as we know from Fig. 4.15. Remarkably all Q factors are higher at 1 T than at zero field which possibly ties back to freezing out energy draining modes by polarization in a magnetic field.

It becomes even more interesting when we regard the performance of the resonator at $B = 0\,\mathrm{T}$ *after* sweeping back from 1 T, while the magnet leads are still connected to the sample. The f_r is back to its original $B = 0\,\mathrm{T}$ value, an expected result of superconductivity having been restored to the entirety of the sample. However, all quality factors are higher than they were at the start of this experiment, albeit now not as large of a difference as between the $B = 0\,\mathrm{T}$ and 1 T situations. If we now short the magnet leads and perform a thermal cycle ($T > T_c$ and back to fridge base temperature), the Q_l and Q_i at least a factor of 2 larger than at $B = 1\,\mathrm{T}$, where the Q_c and Q_e remain relatively constant. The former is an unexpected result and insofar no reason for this increase has been established.

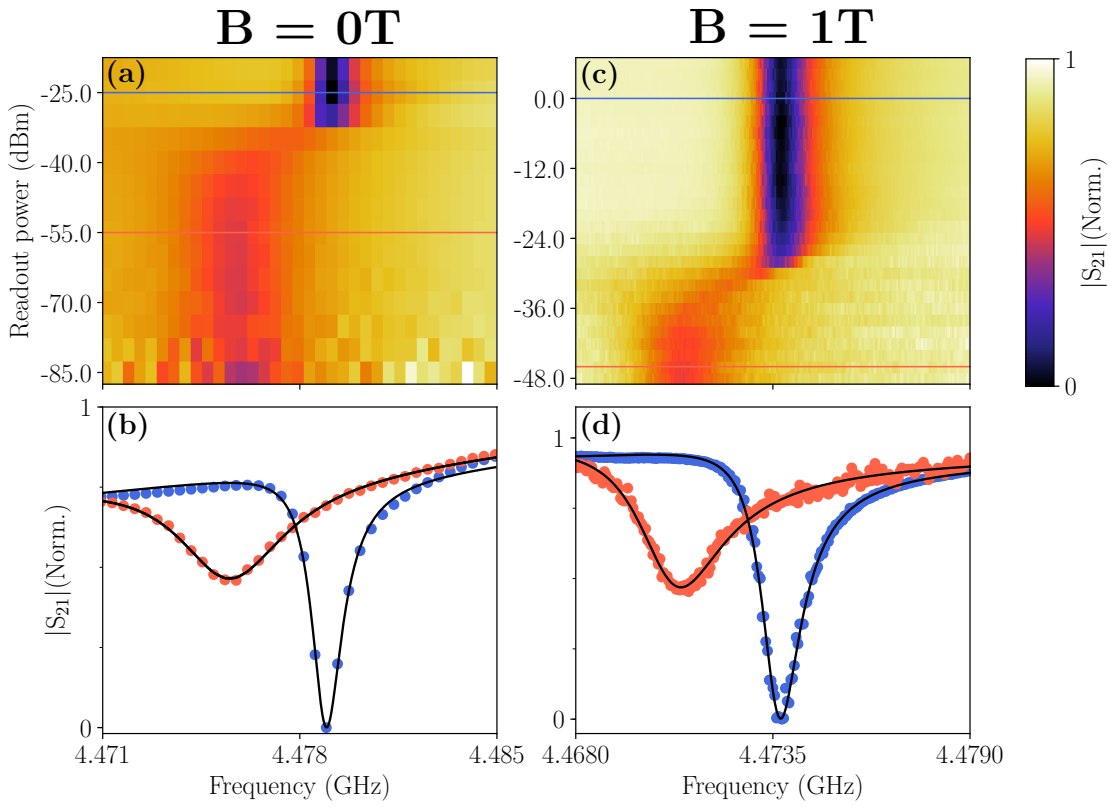

Figure 4.9: (a) Normalized $|S_{21}|$ as function of readout power and frequency for the resonator coupled to the qubit at $B_{||} = 0\,\mathrm{T}$ and (c) $B_{||} = 1\,\mathrm{T}$ with two linecuts at (b) $P_\mathrm{high} = -25\,\mathrm{dBm}$ and $P_\mathrm{low} = -55\,\mathrm{dBm}$ and (d) $P_\mathrm{high} = 0\,\mathrm{dBm}$ and $P_\mathrm{low} = -46\,\mathrm{dBm}$ which are shown together with their fit as solid line. The powersweep at $B_{||} = 0\,\mathrm{T}$ has been performed at $V_\mathrm{gate} - V_\mathrm{CNP} = 167.4\,\mathrm{mV}$, where we observe a $\delta \approx 3\,\mathrm{MHz}$. For $B_{||} = 1\,\mathrm{T}$, the $V_\mathrm{gate} - V_\mathrm{CNP} = 210\,\mathrm{mV}$, where we observe a $\delta \approx 2.75\,\mathrm{MHz}$

Table 4.2: Fit parameters extracted from Eq. 2.51 at single-photon level readout power resonator S_{21} traces in several situations. We analyzed resonator traces at 0 and 1 T, of which linecuts are shown in Fig. 4.9. Furthermore, we regarded $B = 0\,\mathrm{T}$ after sweeping back from 1 T, while the magnet leads were connected (to the current source). Lastly, we have shorted the magnet leads and performed a fridge warmup ($T > T_c$) to expel any vortices left over from the applied magnetic field. Resonator $|S_{21}|$ traces of the two latter situations are shown in Fig. 4.10

Fit parameter	**B = 0 T (leads shorted)**	**B = 1 T**	**B = 0 T after 1 T (leads connected)**	**B = 0 T after 1 T after warmup (leads shorted)**
f_r	4.475 GHz	4.470 GHz	4.475 GHz	4.478 GHz
Q_l	938	1486	1112	3299
Q_i	1070	1784	1265	5077
Q_c	7619	8901	9162	9416
Q_e	7508	8092	9159	8866

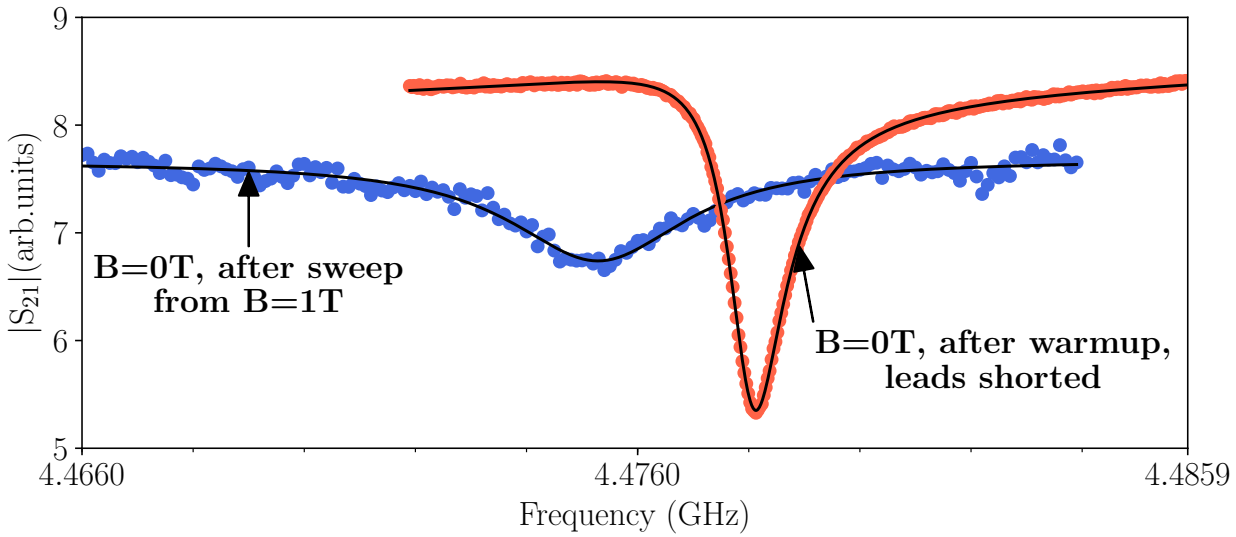

Figure 4.10: $|S_{21}|$ in arbitrary values (to conserve the comparability of both traces in magnitude) as function of frequency for the same resonator in two situations: 1. $B = 0\,\mathrm{T}$ after sweeping back from 1 T, while the magnet leads were connected (to the current source) 2. After the previous situation, performed a fridge thermal cycle ($T > T_c$) to expel any vortices left over from the applied magnetic field and shorted the magnet leads.

4.2.3.2 Resonator gatesweep

To prove that the two-level system we observe here is still the graphene qubit we again regard f_r as function of changing V_gate, shown in Fig. 4.11. Indeed, the resonator is tunable with the gate, indicating our graphene qubit is, thus far, responsive.

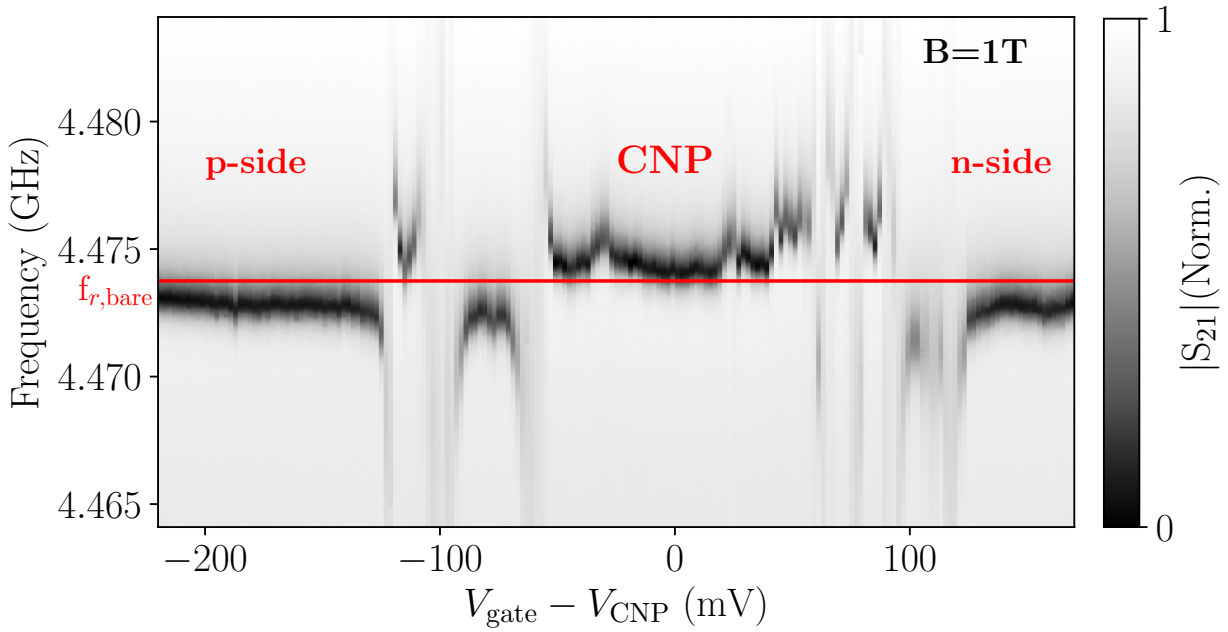

Figure 4.11: S_{21} transmission CW measurements centered around the $f_{r,\mathrm{bare}}$ as function of applied qubit gate voltage offset from the graphene's CNP at $B_{||} = 1\,\mathrm{T}$. From the observed S_{21} transmissions we see that there is a changing amount of level repulsion, thus f_q changes with changing V_{gate}, confirming that the graphene qubit is gate tunable.

4.2.3.3 Qubit spectroscopy at B = 1 T

We continue with two tone CW qubit spectroscopy to obtain $\left|S_{21}^{dist}\right|$, the change in S_{21} of the resonator at a fixed f_r from the dispersive shift of exciting the qubit to its $|1\rangle$ state (see the transmon Hamiltonian Eq. 2.57). The $\left|S_{21}^{dist}\right|$ is of Lorentzian shape around the f_q, which we optimize by both changing readout and qubit drive power such that we reach a middle ground in decreasing the linewidth of the Lorentzian peak and having as large a amplitude as possible. Two qubit spectroscopy traces are shown in Fig. 4.12 for two different gate voltages, one for $f_q < f_r$ and $f_q > f_r$.

From the linewidth σ of the Lorentzian we can estimate the T_2 of the qubit with $T_2 \approx 1/\sigma$, which results in the T_2 to lie between 2.5 and 6 ns for the qubit just above and below the resonator, respectively.

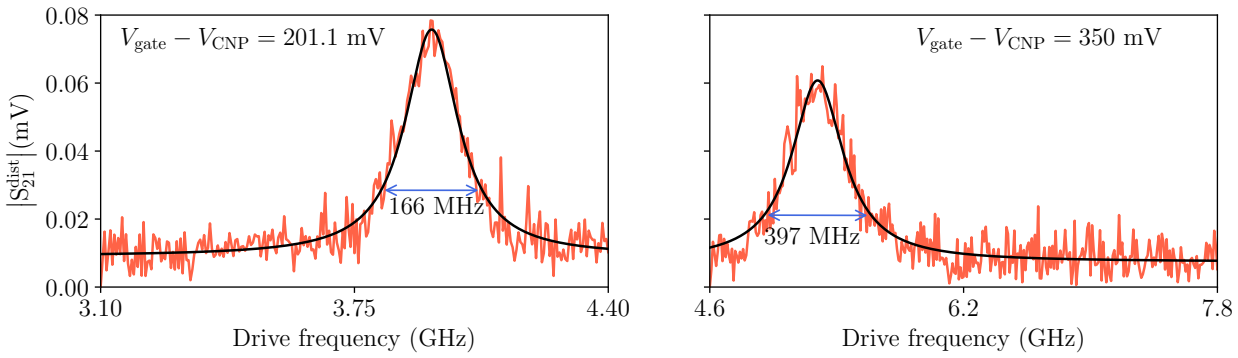

Figure 4.12: Two examples of $\left|S_{21}^{dist}\right|$ measurements from two tone spectroscopy of the graphene qubit with their Lorentzian fit (smooth solid black line), one spectroscopy for $f_q < f_r$ and one for $f_q > f_r$. From the Lorentzian linewidths we estimate the qubit T_2 to lie between 2.5 and 6 ns.

4.2.3.4 Qubit spectroscopy with gate tuning at B = 1 T

As we now know that we can pulse the qubit and observe a 0-1 transition at a specific gate value, we continue with qubit spectroscopy as function of V_{gate} as shown in Fig. 4.13. From this measurement we see that the qubit frequency is gate tunable from 3-7 GHz, with confirmation that there is only one Lorentzian in $\left|S_{21}^{dist}\right|$ per gate value for the entire 3.2-7 GHz range.

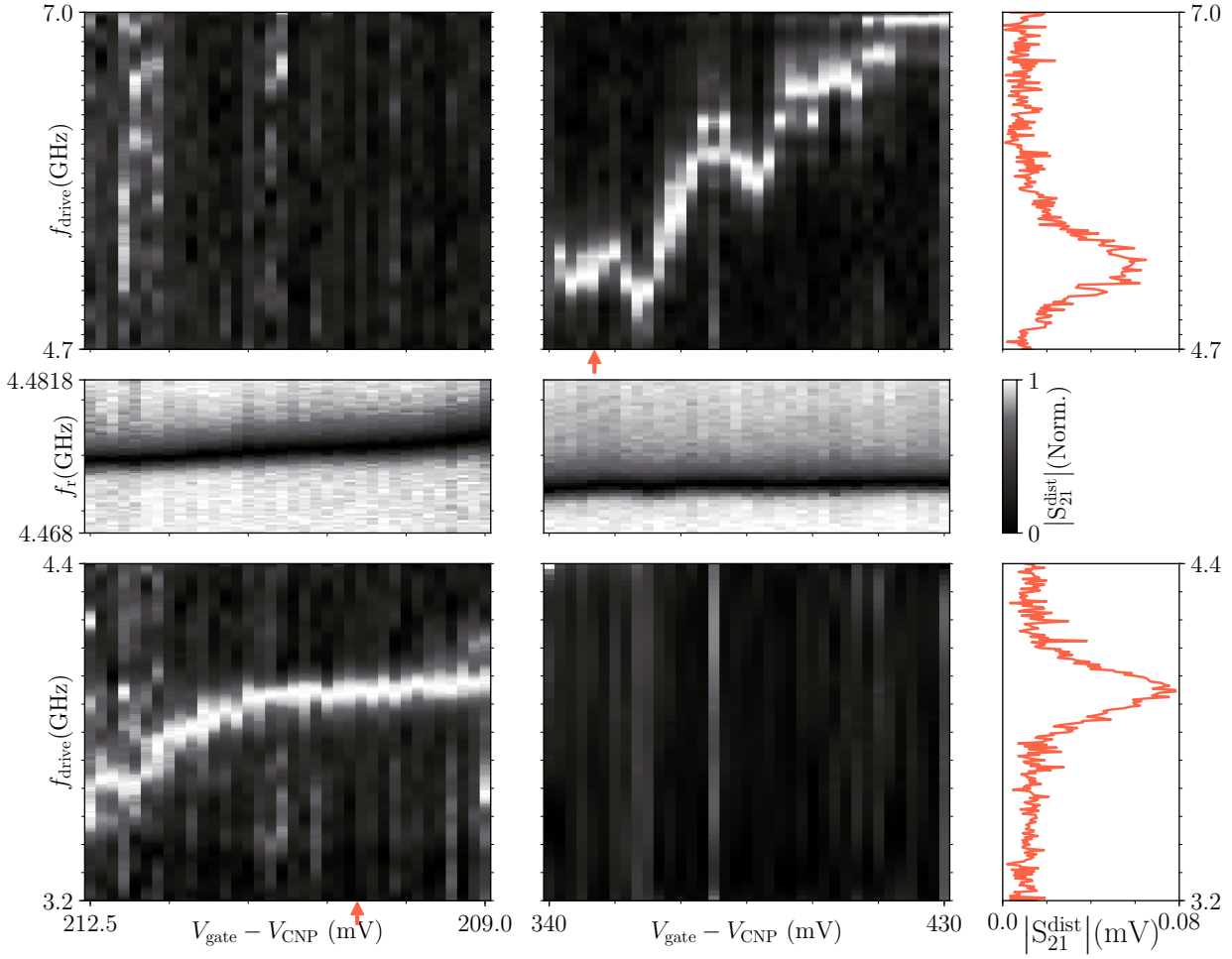

Figure 4.13: (a)(c)(d)(f) Qubit spectroscopy as function of applied gate voltage, where the qubit is moved from around 3.6-4 GHz in (c) and between 4.7-7 GHz in (d), showing in (a) and (f) that there is only one Lorentzian-like increase in S_{21}^{dist} per gate value for the entire 3.2-7 GHz range. The resonator at single-photon level readout is shown in (b) and (e), where an increase in f_r is visible for an increasing f_q. In addition to that, the qubit spectroscopy traces from Fig. 4.12 are added in (g) and (h). For clarity toward the reader, the data shown here is both normalized and filtered using a Savitzky-Golay filter.

The next step of qubit spectroscopy would be to move from continuous wave (CW) to time domain (TD), this however proved to be impossible. No qubit peaks have been found for a range of different drive and readout pulse lengths and timings. The fact that TD qubit spectroscopy yielded no useful results shows that the T_1 of the qubit is smaller than the resolution with which we are able to measure it.

4.2.3.5 Discussions

Observing a qubit peak at $B_{||} = 1\,\text{T}$ is unique and has, to the knowledge of the author, not been published before. Being able to change the frequency of this peak confirms that we have observed an two-level system

with graphene as the normal metal in the Josephson junction. However, these measurement were performed with continuous wave spectroscopy, which renders us immune to any qubit energy leakage that manifests itself in T_1. We have estimated T_2 to lie between 2.5 and 6 ns in CW spectroscopy, which is an impressive number considering the fact this was achieved in $B_{||} = 1\,\mathrm{T}$.

The fact that TD qubit spectroscopy yielded no useful results shows that the T_1 of the qubit is smaller than the resolution with which we are able to measure it. There are several reasons why TD spectroscopy yielded no results. Firstly we identify the gate dielectric as most important (possible) culprit. To overcome the so-called 'standing edges' from the MoRe leads resulted in a necessary 120 nm thick SiN. As SiN is known to be a dielectric with charge-defects, applying a gate voltage to the Josephson junction could be unstable as charges move in the dielectric, changing the electric field on the graphene. This causes an instability in f_q, resulting in an uncertainty in qubit energy and this translates to a low T_2.

Secondly, the qubit might suffer from quasiparticle poisoning as possibly the induced superconducting gap from the NbTiN inside the graphene junction is soft in contrast to epitaxial Al, which is used in the latest generations of high T_1 nanowire superconducting qubits [70]. The presence of quasiparticles enhances the normal current through the Josephson junction, causing dissipation.

Furthermore, the Q_c of the resonator is relatively high, i.e. the timescale of communication with the resonator might be slower than the decay time of the qubit. Lowering the Q_c could therefore be beneficial in future devices.

Finally, the resolution of the AWG (arbitrary waveform generator) used to create the drive and readout pulses in time domain spectroscopy sets a limit on the minimum decay times that can be resolved. In the used measurement setup this resolution is a few nanoseconds, depending on the necessary width of the Gaussian pulses.

4.2.3.5.1 Qubit spectroscopy with gate tuning

As the reader has seen, the data presented in Fig. 4.13 is filtered using a Savitzky-Golay filter. This particular filter was chosen because we needed to smoothen few-point irregularities without destroying the general trend of the signal as function of frequency (the qubit peak had to remain visible). To show why filtering was needed, we show the normalized qubit spectroscopy as function of gate voltage in Fig. 4.14 (normalization is needed to correct for low-frequency changes in S_{21} that manifest as offset). It was needed to increase the qubit drive power to preserve the qubit peak height as f_q moves further away from f_r. When one drives the qubit 'harder', off-qubit-resonance noise is also amplified, which can obscure the qubit peak. Simultaneously, in the >6 GHz regime we suffer from always present in-line resonances that are excited because of the previously mentioned increase in qubit drive power. These emerge every $\sim 160\,\mathrm{MHz}$, which could correspond to a coax cable length of $\sim 1.3\,\mathrm{m}$ or 4.3 feet. This resonance has been observed in other experiments in the same fridge as well, which strengthens the postulate that an in-line coax cable resonates for higher drive powers. To date we have not been able to retrieve the exact origin of the resonances.

4.2.3.5.2 E_J/E_C ratio

No two-photon 0-2 transitions could be detected with this measurement setup, as we were unable to drive the qubit with a higher drive power without exciting the above described resonances in line, obscuring qubit peaks. Since no two-photon 0-2 transitions have been observed, we were unable to determine the E_J/E_C ratio of this qubit. Even if we had fabricated devices with SIS Al/AlOx junctions that use the same transmon capacitor plate geometry, we could have not been able to determine the E_C accurately, as research has shown that an SNS junction can reduce the E_C of the qubit in a, so far, unpredictable way [70, 71].

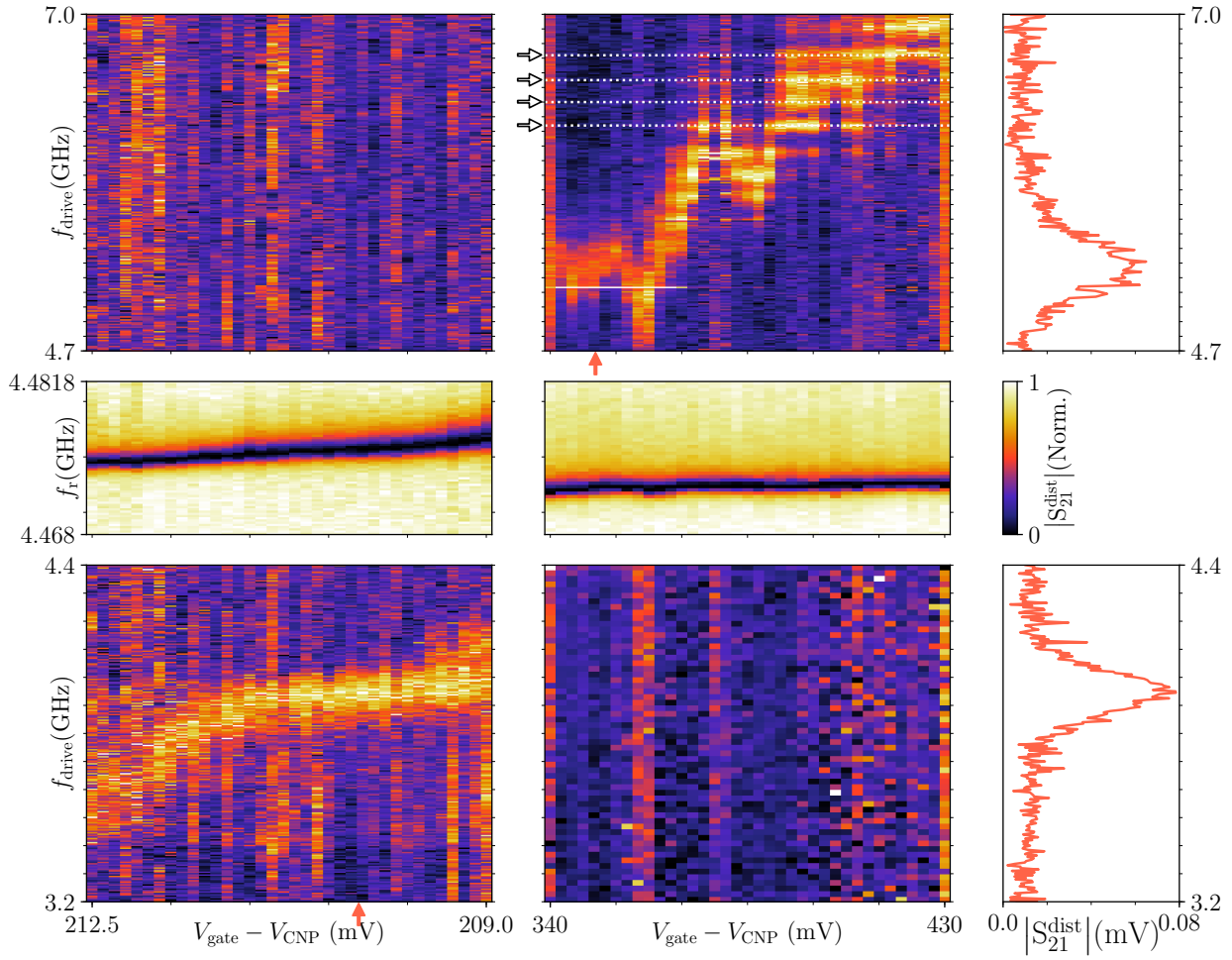

Figure 4.14: (a)(c)(d)(f) Qubit spectroscopy as function of applied gate voltage, where the qubit is moved from around 3.6-4 GHz in (c) and between 4.7-7 GHz in (d), showing in (a) and (f) that there is only one Lorentzian shape increase in $\left|S_{21}^{dist}\right|$ per gate value for the entire 3.2-7 GHz range. The resonator at single-photon level readout is shown in (b) and (e), where an increase in f_r is visible for an increasing f_q, a change in level repulsion. In addition to that, the qubit spectroscopy traces from Fig. 4.12 are added in (g) and (h). The data shown here is normalized only. Highlighted in (d) with white dotted lines and arrows are the in-line resonances that emerge with higher qubit driving power, which are separated by ~ 160 MHz. The white horizontal line in (d) at 5 GHz that crosses the qubit peak is from an additional on-chip resonator with that exact resonance frequency.

4.2.3.6 Qubit frequency as function of magnetic field

After the exhaustive efforts taken to produce the previous high quality CW measurements and tedious tuning to observe useful TD measurements, it was decided to investigate qubit spectroscopy frequency as function of $B_{||}$. In the sweep going *up* in magnetic field resonance traces were taken at high and low readout power, therefore recording the level repulsion at each magnetic field (for a fixed V_{gate}). From that we can estimate f_q using Eq. 2.70, where we can now use a calculated g value extracted from the CW qubit spectroscopy, calculated using

$$\delta = f_{r,\mathrm{bare}} - f_r = 4.473 - 4.475 \text{ GHz}$$
$$\Delta = f_q - f_{r,\mathrm{bare}} = 3.772 - 4.473 \text{ GHz}$$
$$g/2\pi \approx \frac{\sqrt{\delta\Delta}}{2\pi} = 33.4 \text{ MHz}.$$

Then, using g, we can calculate f_q following the above equations when we know both $f_{r,\text{bare}}$ and f_r. Both δ and f_q as function of parallel magnetic field is shown in Fig. 4.15(a). The trend of these two parameters are exactly opposite, but are presented to the reader to illustrate their order of magnitude change with magnetic field.

At the same time we track $\Delta f_r/f_r$ in Fig. 4.15(b) as function of field that reduces with increasing field in the same parabolic fashion of $-kB_{||}^2$, but a better fit is obtained with adding another degree of freedom with $-kB_{||}^2 - k'B_{||}$. The takeaway message is the same: A parabolic relationship between applied parallel magnetic field and $\Delta f_r/f_r$ is observed.

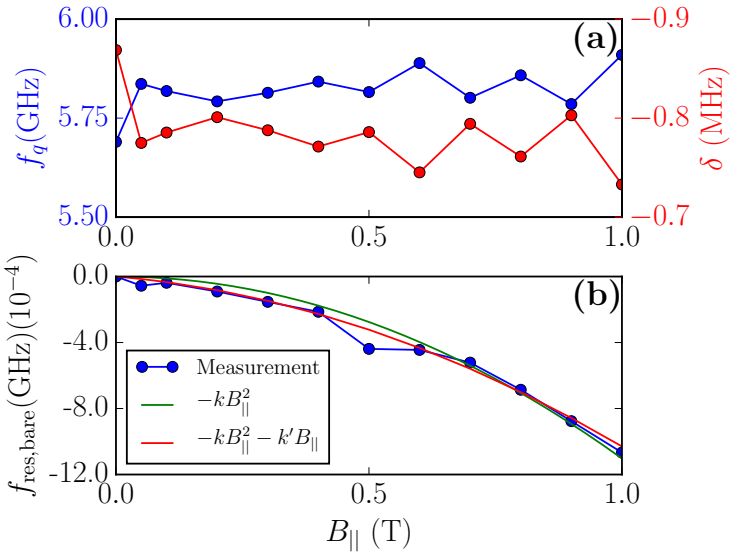

Figure 4.15: (a) The measured qubit frequency and derived δ using Eq. 2.70 as function of magnetic field. The trend of these two parameters are exactly opposite, but are presented to the reader to see their order of magnitude change with magnetic field. (b) The dependence of the relative change in f_r as function of $B_{||}$ is shown from measurement data, the fit to $-kB_{||}^2$ with $k = 1.1 \times 10^{-3}\,\text{T}^{-2}$ and fit to $-kB_{||}^2 - k'B_{||}$ with $k = 7.7 \times 10^{-4}\,\text{T}^{-2}$, $k' = 2.6 \times 10^{-4}\,\text{T}^{-2}$.

The change in f_q for changing field is within a range of $\sim 200\,\text{MHz}$, which could possibly be attributed to the fluctuations of charge density of the graphene or due to a change in kinetic inductance of the capacitor plates. In any case, no direct discernible relationship has been found between field strength and f_q that is decoupled from V_{gate}.

4.2.3.7 Back at zero magnetic field

We have swept the $B_{||}$ back to 0 T, where we performed CW qubit spectroscopy once more after a thermal cycle ($T > T_c$ and back to base temperature) and shorting the magnet leads. This time, we do observe a peak in $\left|S_{21}^{dist}\right|$, which we compare directly to the qubit peak observed at $B_{||} = 1\,\text{T}$ as both spectroscopies were taken at the same V_{gate} value. The f_q at 0 T is $\sim 20\,\text{MHz}$ lower than the qubit frequency at 1 T and the linewidth of the Lorentzian peak at 0 T is 85 MHz smaller than its peak at 1 T.

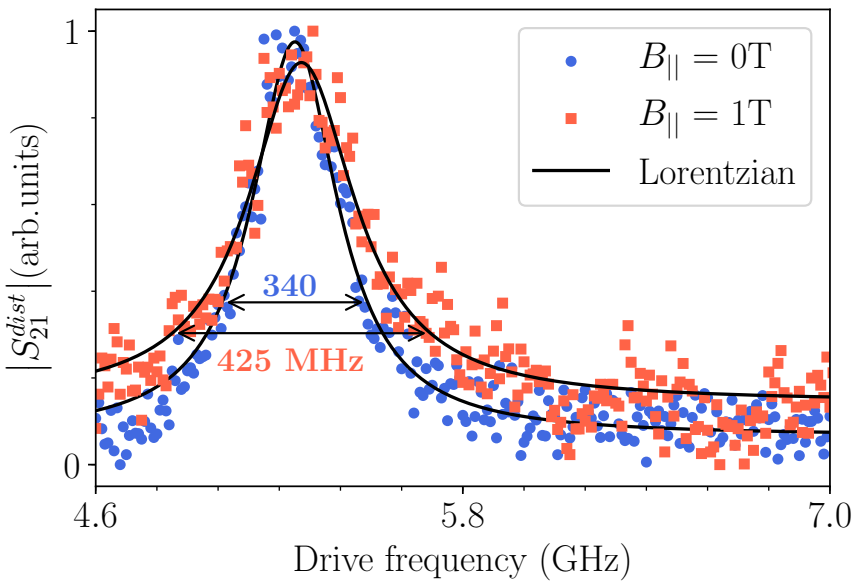

Figure 4.16: $|S_{21}^{dist}|$ as function of qubit drive frequency for $B_{||}$ =0 in blue dots and 1 T in red squares, with their respective Lorentzian fit as solid line. The V_{gate} has been kept constant between these two measurements. At $B_{||} = 0$ T the fridge has had a thermal cycle and magnet leads were shorted.

It is remarkable that after being at $B_{||} = 1$ T we observe a qubit peak at 0 T. The linewidth is 85 MHz smaller in zero field, which seems logical as the magnetic field should be a disturbance in the resonator-qubit system. This is also in line with the discovery that the Q_i of the resonator is much larger with the system in this exact configuration.

4.2.3.8 Reloading sample

All previous measurements have taken place at the first load of the sample in the fridge. Afterwards the sample was taken and moved into a room temperature vacuum desiccator and kept there for several weeks. In an attempt to retake measurements at $B = 0$ T, the sample was loaded a second time. As we have done before, one of the first measurements is a resonator readout powersweep, which shows in Fig. 4.17 a different behavior than we have seen before. A kink in $|S_{21}|$ is visible for readout powers above -13 dBm which moves up in frequency for increasing readout power. A similar kink is visible below -14 dBm that has the same frequency and power dependence. This same kink has been seen in the first load as well, albeit not as pronounced as it is now.

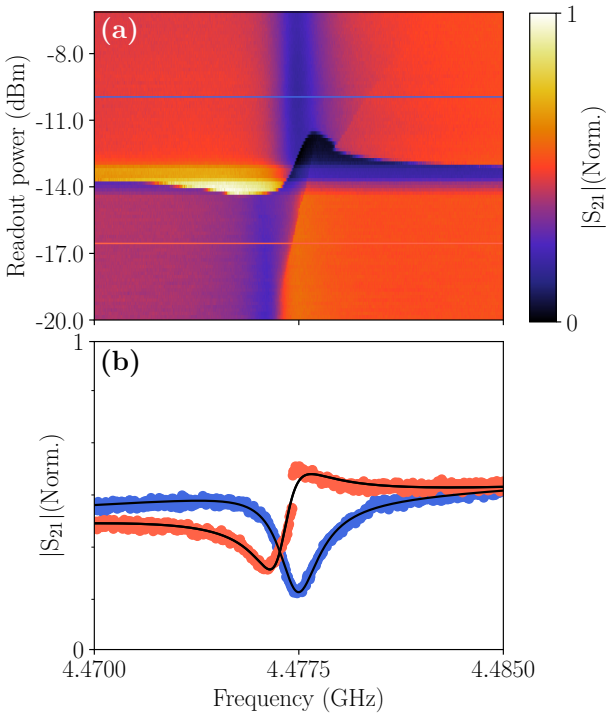

Figure 4.17: (a) Normalized S_{21} as function of readout power and frequency for the resonator coupled to the qubit at $B_{||} = 0\,\mathrm{T}$ after being in room temperature and vacuum for several weeks. Two linecuts at $P_{\mathrm{high}} = -9.8\,\mathrm{dBm}$ and $P_{\mathrm{low}} = -16.4\,\mathrm{dBm}$ are shown in (b) together with their fit as solid line. This powersweep has been performed at a grounded gate voltage.

Storing the sample in a vacuum desiccator at room temperature apparently does not fully protect (at least) the resonators from a form of degradation. The resonances have become more asymmetrical, which could be a sign of sample degradation. This degradation has been observed in different samples, although the origin of this remains unknown.

4.3 Results: Simulations

We know that the E_J of graphene Josephson junctions is reliably tunable by changing junction geometries, however no such method has been utilized in this research group before to target a certain charging energy E_C. As E_C is needed in order to accurately aim for a large enough ratio of E_J/E_C, it was decided to investigate if FEM simulations could accurately determine the C_Σ of a qubit-resonator system. To check the accuracy of the E_C values from the simulations, the E_{01} and E_{02} of Al/AlOx transmon qubits have been measured in $B = 0\,\mathrm{T}$. This conventional transmon is easy to fabricate and it has been shown that its E_{01} and E_{02} can be measured. Since the geometry has the largest influence on the value of C_Σ, thus E_C, we gain useful information for the graphene qubit system from these simpler to fabricate SIS transmon qubits.

4.3.1 Extracting E_c

It is not possible to directly measure E_c, the only quantities that we can measure of the qubit that allow us to calculate E_c are its energy levels. The f_q, that we have found for the graphene qubit, is its E_{01} transition energy. The qubit is constantly (in CW measurement) excited to its E_1 which costs an amount of E_{01}. If the average number of photons being pumped in the resonator-qubit system is increased by orders of magnitude from the single-photon level, a two-photon process can occur that together has energy E_{02}, bringing the qubit into its second excited state. We can recognize such a transition in the qubit spectroscopy traces as a second Lorentzian shaped peak that appears at high qubit drive power at a frequency $\frac{E_{02}}{2}$. We can extract E_c in two different ways from these energy levels. Firstly, we could use the anharmonicity approximation from the transmon Hamiltonian of Eq. 2.61 and use $E_{12} = E_{02} - E_{01}$ to immediately calculate $E_C = E_{01} - E_{12}$, required that $E_J/E_C \gg 1$, or to be more precise, $E_J/E_C \sim 50$. Since both E_J and E_C can differ from the designed values, we are unsure whether or not the value for this ratio is around 50, and thus unsure if we are allowed to use this approximation. To be certain, we would have to calculate both E_J and E_C and compute their ratio, which brings us back to the first problem. That brings us to the second method: Solve the transmon Hamiltonian for a large enough n and numerically find the combination of E_J and E_C that comes closest to the measured E_{01} and E_{02}. This method can be employed irrespective of the values of E_J and E_C and is therefore used in further analysis. An example of a qubit spectroscopy and drive powersweep is shown in Fig. 4.18, showing the power broadening of the qubit spectroscopy peaks as well as the multiple energy levels that are accessed by multiple photon processes.

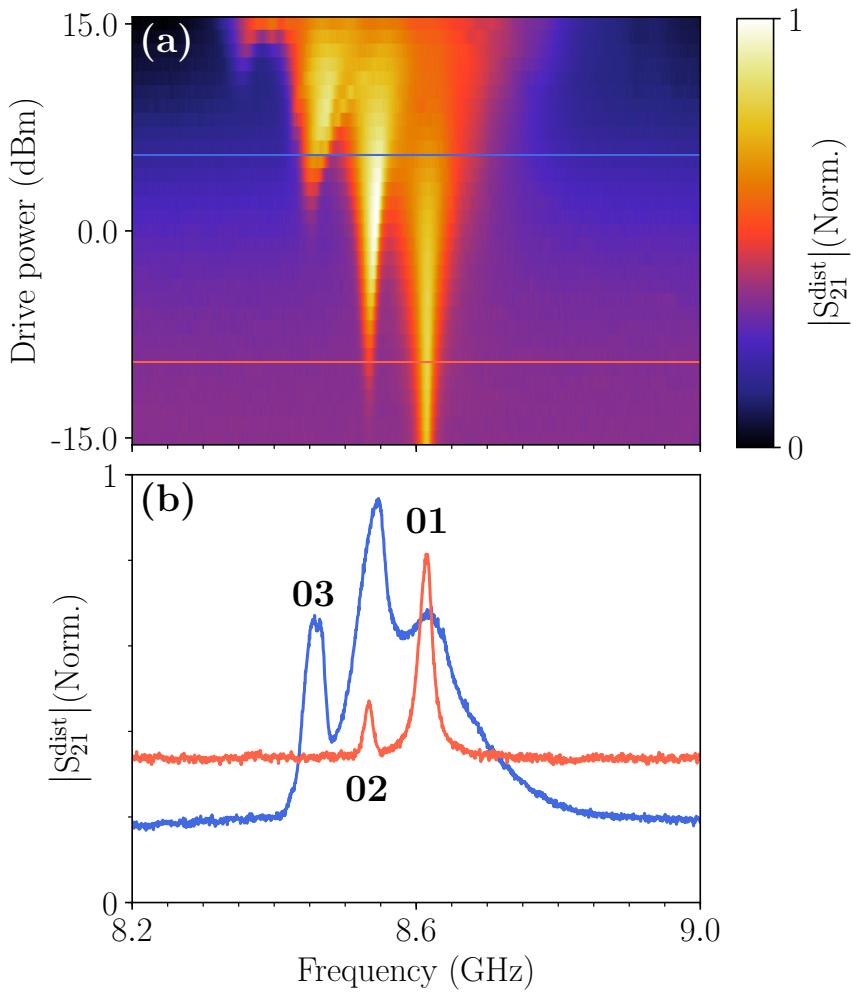

Figure 4.18: (a) Qubit spectroscopy for a drive powersweep, with two linecuts shown in (b) at 5 and -10 dBm. We observe the E_{01} qubit peak power broadening with increased drive power and the two-photon E_{02} and three-photon E_{03} peaks increasing in amplitude and linewidth for increased power.

We now find the E_J and E_C in a semi-brute force manner by calculating both E_{01} and E_{02} using Eq. 2.57 for a range of E_C values and an E_J that minimizes the difference between e.g. $E_{01,\text{calc}} - E_{01,\text{meas}}$, which is performed using the Newton-Raphson method. Since there is a unique E_J,E_C pair that results in the particular E_{01} and E_{02} that is measured, but there is a whole range of E_J,E_C pairs that can result in E_{01} or E_{02}, we look for the intersection between the E_J,E_C function per energy transition shown in Fig. 4.19. The error in E_J and E_C can be as low as ~ 100 Hz within reasonable computation time.

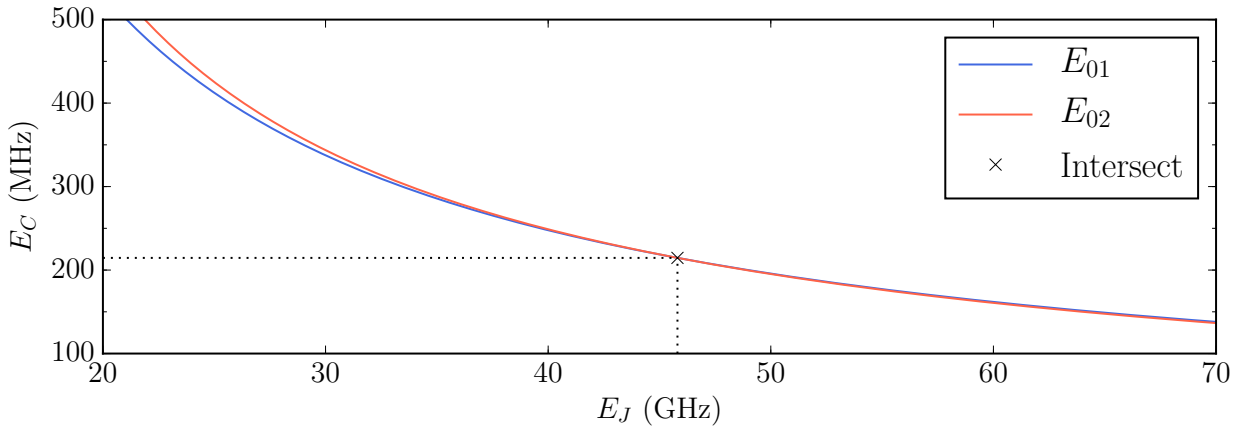

Figure 4.19: Graphical representation of determining the unique pair of E_J,E_C that corresponds to a measured qubit. The curves separately represent E_J,E_C values that result in the $E_{01,\text{meas}}$ or $E_{02,\text{meas}}$, calculated from Eq. 2.57. The intersection of both of these curves determines the unique E_J, E_C pair.

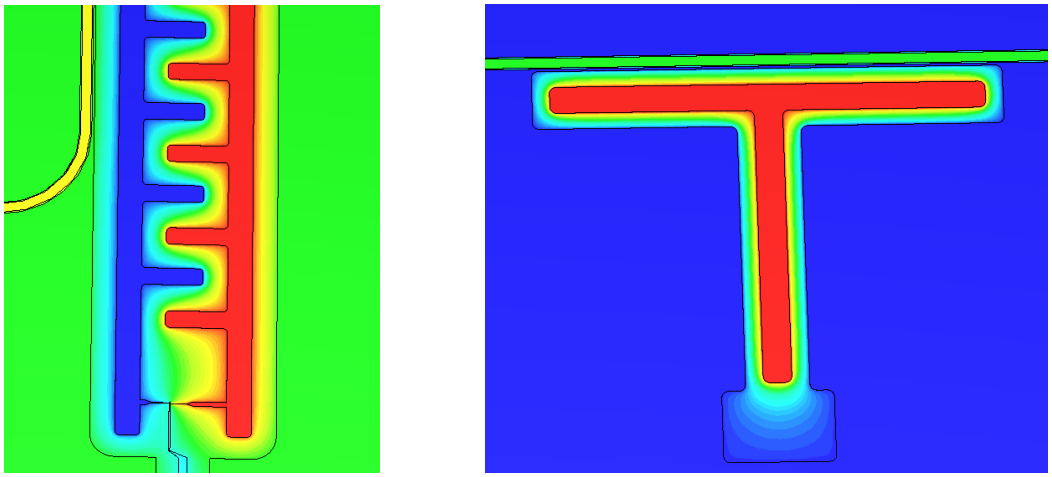

(a) E-shape (b) T-shape

Figure 4.20: Examples of the two different transmon shapes that have been measured and simulated.

4.3.1.1 Measurement and simulation comparison

We have measured and simulated two transmon geometries, a T-shape and a finger capacitance shape, which we shall call an E-shape. Examples of these geometries are shown in Fig. 4.20. The measured qubits, their extracted energy parameters and E_C found through simulation using both the RF solver and E-static solver methods, is presented in Table 4.3

The RF solver and E-static solver methods can both come close to the actual value of E_C, although there was no way of knowing in advance which of the two would. However, the simulations are still off by $\sim$ 13-27 MHz in the best to worst case, choosing the value from the solver that gave the closest result. Even though this is close enough to be used in the design process, there is no way of knowing in advance which solver method finds the closest E_C.

The difference in numerically extracted and simulated E_C is thought to arise from not taking into account the enhanced surface impedance from using a thin-film system. The surface impedance was added to all simulations but yielded approximately the same results (within a few MHz). We are aware of other research groups being able to simulate E_C accurately within 10 MHz using the same software program, with the difference that superconducting films of $\sim$ 200 nm are used. This strongly suggests that the thickness of the

film is an important factor for the software to accurately determine the capacitance of the system, although in which way exactly remains unknown.

Table 4.3: Results from measurement of the E_{01} and E_{02} transition of two T-shaped and two E-shaped Al/AlOx transmons, with calculations of E_J, E_C and their ratio through the estimation presented in Eq. 2.62, 2.63. The numerically extracted values of E_J, E_C and their ratio calculated using the method described in this section is compared to the values of E_C obtained from the FEM simulations performed with CST Studio Suite®, either directly from the RF measurements or from the capacitance matrix obtained from E-static solver and converted to E_C using Eq. 3.1. Highlighted are the simulated E_C's that come closest to the measured values.

Measurement			Extracted parameters						Simulation	
Shape	**Qubit transistion**		**Estimation**			**Numerical solution**			**E_C**	
	E_{01}(GHz)	**E_{02}**(GHz)	**E_C**(MHz)	**E_J**(GHz)	**E_J/E_C**	**E_C**(MHz)	**E_J**(GHz)	**E_J/E_C**	**RF**	**E-static**
T	4.29	8.26	312.6	7.35	23.53	263	9.91	37.62	233	250
T	8.648	17.07	228.8	40.86	178.6	216	45.6	211.8	243	279
E	7.84	15.20	490.6	15.7	31.9	425	20.23	47.6	366	442
E	7.36	14.3	450.6	15.0	33.4	392	19.3	49.3	367	442

4.3.1.2 Al/AlOx transmon Time Domain measurements

As time domain qubit spectroscopy is quite a delicate measurement with many parameters than can be changed, it is instructive to be able to do this for the Al/AlOx transmon that we *know* works, such that we can apply the skills gained here in measuring the graphene qubit. Furthermore, we wanted to confirm a correctly working experimental setup.

We were able to drive the qubit into its $|1\rangle$ state by using time domain pulsing, and obtained a linewidth of $\sigma \approx 1.4\,\text{MHz}$ shown in Fig. 4.21, which would indicate a $T_2 \approx 700\,\text{ns}$. Furthermore, we were able to measure the T_1 and T_2 of this particular transmon, as shown in Fig. 4.22

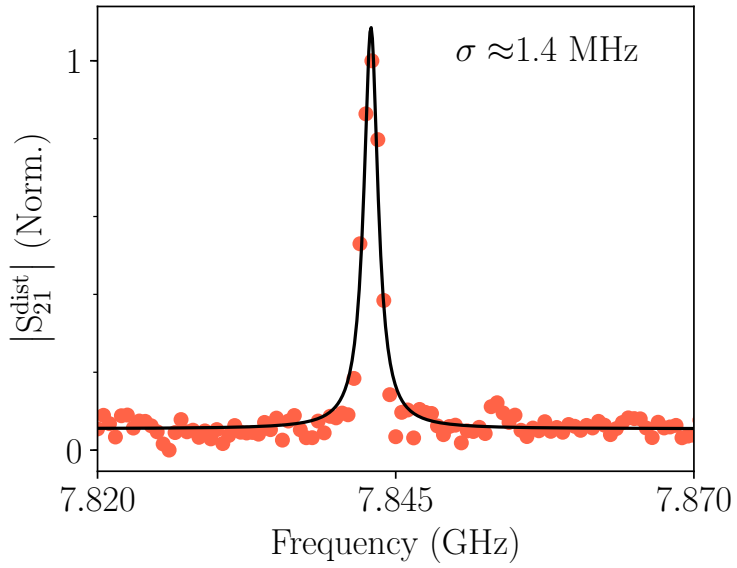

Figure 4.21: Normalized qubit spectroscopy for an Al/AlOx transmon and its Lorentzian fit.

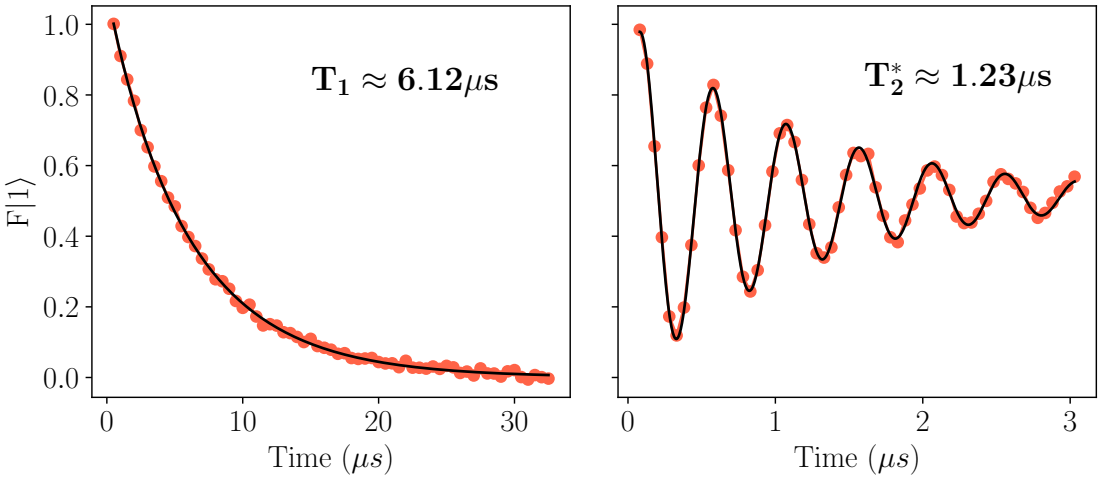

Figure 4.22: Measurement of T_1 and T_2^*, with the weight of the $|1\rangle$ state on the vertical axis.

4.4 Outlook

4.4.1 Magnetic field insensitive resonators

The magnetic field insensitive superconducting resonators will be useful in any experiment that employs cQED and either require a magnetic field or suffer from magnetic field noise. This would particularly be useful in topological devices and spin-qubit systems.

4.4.2 Graphene transmon

We are at the forefront of utilizing graphene in a transmon qubit, however there is a lot of room for improvement in terms of qubit performance. As we want to move to time domain measurements, the T_1 and T_2 lifetimes of the qubit have to be enhanced. We have identified the lossy dielectric SiN as possible culprit for charge jumps, adding charge noise to f_{q}. Using a cleaner dielectric (such as hBN) between the gate and junction could decrease the qubit energy uncertainty and increase T_2 accordingly[1]. Furthermore, it is necessary to investigate if the induced superconducting gap in the graphene junction is too soft, a problem that could be solved by optimizing contact recipes and materials. A possible improvement in T_1 is the possible existence of vortices in the transmon capacitor plates, especially when changing the magnitude of the magnetic field, a misalignment in the parallel to plane field can quickly become a source of vortices. Adding vortex pinning sites to the plates as is implemented in the rest of the NbTiN film should prevent this, however we need to show it does not influence any other parameter negatively.

Furthermore, E_{02} transitions have not yet been measured. It is instructive to find with E_{02} the anharmonicity of the graphene transmon, as this could be different from what has been seen so far for 'conventional' Al/AlOx transmons.

When the qubit lifetimes are increased significantly, coherent state control becomes possible. This would enable parity measurements to be performed [20], allowing us to study parity fluctuations as function of magnetic field in systems of interest (topological qubit experiments).

[1]Fabrication of a graphene qubit with hBN as dielectric for the gate has been attempted. However, this qubit was not gate tunable, even though it was intended to be, which was postulated to be the result of an airgap between the dielectric and the junction because of standing edges of the MoRe leads.

Chapter 5

Conclusions

We have investigated the performance of hole patterned CPW resonators in an applied perpendicular magnetic field. We found that increased hole density increases the amount of vortices that can be trapped. We can accurately predict the magnetic field threshold after which the vortex pinning sites are saturated up to ρ_{hole} =7.2 µm^{-2}. This saturation shows itself as a significant decrease in Q_i. At a magnetic field larger than B_th, we observe an additional reduction of Q_i when increasing the readout power. This reduction confirms readout power dependent dissipation channels through free moving vortices, when vortex pinning sites are saturated. Moreover, the results in this thesis show that hole patterned CPW resonators can be used in parallel magnetic field of several Teslas, as well as perpendicular fields up to 35 mT for $\rho_{hole} = 28.9\,\mu\mathrm{m}^{-2}$.

By implementation of these resonators, we have described the successful continuous wave qubit spectroscopy of a graphene transmon qubit at $B_{||} = 1$ T with a minimal linewidth of 166 MHz and demonstrated manipulation of the qubit frequency between 3.2-7 GHz with electric field. This is the first ever measured superconducting qubit that shows these properties at a magnetic field of 1 T.

Furthermore, we have measured E_{02} transitions for several conventional Al/AlOx transmons and determined their E_C numerically. We have compared FEM simulated E_C values, using two different solver methods, to the experimentally extracted values. It was inconclusive which solver method is more reliable.

Finally, to confirm a correctly working experimental setup for time domain measurements, successful T_1 and $T_2^\star$ measurements of a Al/AlOx transmon have been performed.

Bibliography

[1] Microsoft, "Microsoft doubles down on quantum computing bet," 2016.

[2] B. Krzanich, "The Promise of Quantum Computing," 2015.

[3] P. Ball, "Google moves closer to a universal quantum computer," 2016.

[4] H. Neven, "Hardware Initiative at Quantum Artificial Intelligence Lab," 2014.

[5] M. H. Devoret, A. Wallraff, and J. M. Martinis, "Superconducting qubits: A short review," *arXiv preprint cond-mat/0411174*, 2004.

[6] L. DiCarlo, J. M. Chow, J. M. Gambetta, L. S. Bishop, B. R. Johnson, D. I. Schuster, J. Majer, A. Blais, L. Frunzio, S. M. Girvin, and Others, "Demonstration of two-qubit algorithms with a superconducting quantum processor," *Nature*, vol. 460, no. 7252, pp. 240–244, 2009.

[7] B. Hensen, H. Bernien, A. E. Dréau, A. Reiserer, N. Kalb, M. S. Blok, J. Ruitenberg, R. F. L. Vermeulen, R. N. Schouten, C. Abellán, and Others, "Loophole-free Bell inequality violation using electron spins separated by 1.3 kilometres," *Nature*, vol. 526, no. 7575, pp. 682–686, 2015.

[8] W. Pfaff, B. J. Hensen, H. Bernien, S. B. van Dam, M. S. Blok, T. H. Taminiau, M. J. Tiggelman, R. N. Schouten, M. Markham, D. J. Twitchen, and Others, "Unconditional quantum teleportation between distant solid-state quantum bits," *Science*, vol. 345, no. 6196, pp. 532–535, 2014.

[9] D. Loss and D. P. DiVincenzo, "Quantum computation with quantum dots," *Physical Review A*, vol. 57, no. 1, p. 120, 1998.

[10] R. Hanson, L. P. Kouwenhoven, J. R. Petta, S. Tarucha, and L. M. K. Vandersypen, "Spins in few-electron quantum dots," *Reviews of Modern Physics*, vol. 79, no. 4, p. 1217, 2007.

[11] M. Freedman, A. Kitaev, M. Larsen, and Z. Wang, "Topological quantum computation," *Bulletin of the American Mathematical Society*, vol. 40, no. 1, pp. 31–38, 2003.

[12] C. Nayak, S. H. Simon, A. Stern, M. Freedman, and S. D. Sarma, "Non-Abelian anyons and topological quantum computation," *Reviews of Modern Physics*, vol. 80, no. 3, p. 1083, 2008.

[13] A. Stern, "Non-Abelian states of matter," *Nature*, vol. 464, no. 7286, pp. 187–193, 2010.

[14] A. Y. Kitaev, "Fault-tolerant quantum computation by anyons," *Annals of Physics*, vol. 303, no. 1, pp. 2–30, 2003.

[15] F. Hassler, A. R. Akhmerov, C. Y. Hou, and C. W. J. Beenakker, "Anyonic interferometry without anyons: how a flux qubit can read out a topological qubit," *New Journal of Physics*, vol. 12, no. 12, p. 125002, 2010.

[16] F. Wilczek, "Majorana returns," *Nature Physics*, vol. 5, no. 9, pp. 614–618, 2009.

[17] V. Mourik, K. Zuo, S. M. Frolov, S. R. Plissard, E. Bakkers, and L. P. Kouwenhoven, "Signatures of Majorana fermions in hybrid superconductor-semiconductor nanowire devices," *Science*, vol. 336, no. 6084, pp. 1003–1007, 2012.

[18] T. Hyart, B. van Heck, I. C. Fulga, M. Burrello, A. R. Akhmerov, and C. W. J. Beenakker, "Flux-controlled quantum computation with Majorana fermions," *Physical Review B*, vol. 88, no. 3, p. 35121, 2013.

[19] J. Alicea, Y. Oreg, G. Refael, F. von Oppen, and M. P. A. Fisher, "Non-Abelian statistics and topological quantum information processing in 1D wire networks," *Nature Physics*, vol. 7, no. 5, pp. 412–417, 2011.

[20] D. Ristè, C. C. Bultink, M. J. Tiggelman, R. N. Schouten, K. W. Lehnert, and L. DiCarlo, "Millisecond charge-parity fluctuations and induced decoherence in a superconducting transmon qubit," *Nature communications*, vol. 4, p. 1913, 2013.

[21] J. D. Sau, R. M. Lutchyn, S. Tewari, and S. D. Sarma, "Generic new platform for topological quantum computation using semiconductor heterostructures," *Physical review letters*, vol. 104, no. 4, p. 40502, 2010.

[22] J. Alicea, "Majorana fermions in a tunable semiconductor device," *Physical Review B*, vol. 81, no. 12, p. 125318, 2010.

[23] R. M. Lutchyn, J. D. Sau, and S. D. Sarma, "Majorana fermions and a topological phase transition in semiconductor-superconductor heterostructures," *Physical review letters*, vol. 105, no. 7, p. 77001, 2010.

[24] Y. Oreg, G. Refael, and F. von Oppen, "Helical liquids and Majorana bound states in quantum wires," *Physical review letters*, vol. 105, no. 17, p. 177002, 2010.

[25] A. Das, Y. Ronen, Y. Most, Y. Oreg, M. Heiblum, and H. Shtrikman, "Zero-bias peaks and splitting in an Al-InAs nanowire topological superconductor as a signature of Majorana fermions," *Nature Physics*, vol. 8, no. 12, pp. 887–895, 2012.

[26] M. T. Deng, C. L. Yu, G. Y. Huang, M. Larsson, P. Caroff, and H. Q. Xu, "Anomalous zero-bias conductance peak in a Nb–InSb nanowire–Nb hybrid device," *Nano letters*, vol. 12, no. 12, pp. 6414–6419, 2012.

[27] S. D. Sarma, J. D. Sau, and T. D. Stanescu, "Splitting of the zero-bias conductance peak as smoking gun evidence for the existence of the Majorana mode in a superconductor-semiconductor nanowire," *Physical Review B*, vol. 86, no. 22, p. 220506, 2012.

[28] Y. Kubo, C. Grezes, A. Dewes, T. Umeda, J. Isoya, H. Sumiya, N. Morishita, H. Abe, S. Onoda, T. Ohshima, V. Jacques, A. Dréau, J.-F. Roch, I. Diniz, A. Auffeves, D. Vion, D. Esteve, and P. Bertet, "Hybrid quantum circuit with a superconducting qubit coupled to a spin ensemble," *Phys. Rev. Lett.*, vol. 107, p. 220501, Nov 2011.

[29] J. Koch, M. Y. Terri, J. Gambetta, A. A. Houck, D. I. Schuster, J. Majer, A. Blais, M. H. Devoret, S. M. Girvin, and R. J. Schoelkopf, "Charge-insensitive qubit design derived from the Cooper pair box," *Physical Review A*, vol. 76, no. 4, p. 42319, 2007.

[30] J. A. Schreier, A. A. Houck, J. Koch, D. I. Schuster, B. R. Johnson, J. M. Chow, J. M. Gambetta, J. Majer, L. Frunzio, M. H. Devoret, and Others, "Suppressing charge noise decoherence in superconducting charge qubits," *Physical Review B*, vol. 77, no. 18, p. 180502, 2008.

[31] V. E. Calado, S. Goswami, G. Nanda, M. Diez, A. R. Akhmerov, K. Watanabe, T. Taniguchi, T. M. Klapwijk, and L. M. K. Vandersypen, "Ballistic Josephson junctions in edge-contacted graphene," *Nature nanotechnology*, 2015.

[32] F. Borsoi, "Magnetic field resilient superconducting circuit elements for Majorana parity detection," 2015.

[33] H. Onnes, "The resistance of pure mercury at helium temperatures," *Commun. Phys. Lab. Univ. Leiden*, 1911.

[34] M. Tinkham, *Introduction to superconductivity*. Dover, second edition ed., 1996.

[35] A. A. Abrikosov, "Magnetic properties of superconductors of the second group," *Sov. Phys.-JETP (Engl. Transl.);(United States)*, vol. 5, no. 6, 1957.

[36] J. Bardeen and M. J. Stephen, "Theory of the Motion of Vortices in Superconductors," *Physical Review*, vol. 140, pp. A1197–A1207, Nov 1965.

[37] C. Song, *Microwave Properties of Vortices in Superconducting Resonators*. PhD thesis, 2011.

[38] P. W. Anderson and Y. B. Kim, "Hard superconductivity: Theory of the motion of abrikosov flux lines," *Rev. Mod. Phys.*, vol. 36, pp. 39–43, Jan 1964.

[39] J. I. Gittleman and B. Rosenblum, "The Pinning Potential and HighFrequency Studies of TypeII Superconductors," *Journal of Applied Physics*, vol. 39, pp. 2617–2621, May 1968.

[40] M. P. A. Fisher, "Vortex-glass superconductivity: A possible new phase in bulk high- T c oxides," *Physical Review Letters*, vol. 62, pp. 1415–1418, Mar 1989.

[41] G. Stan, S. B. Field, and J. M. Martinis, "Critical field for complete vortex expulsion from narrow superconducting strips," *Phys. Rev. Lett.*, vol. 92, p. 097003, Mar 2004.

[42] K. H. Kuit, J. R. Kirtley, W. van der Veur, C. G. Molenaar, F. J. G. Roesthuis, A. G. P. Troeman, J. R. Clem, H. Hilgenkamp, H. Rogalla, and J. Flokstra, "Vortex trapping and expulsion in thin-film $yba_2cu_3o_{7-\delta}$ strips," *Phys. Rev. B*, vol. 77, p. 134504, Apr 2008.

[43] C. Lee, B. Janko, I. Derenyi, and A.-L. Barabasi, "Reducing vortex density in superconductors using the 'ratchet effect'," *Nature*, vol. 400, no. 6742, p. 337, 1999.

[44] D. Bothner, T. Gaber, M. Kemmler, D. Koelle, and R. Kleiner, "Improving the performance of superconducting microwave resonators in magnetic fields," *Applied Physics Letters*, vol. 98, no. 10, p. 102504, 2011.

[45] R. Meservey and P. M. Tedrow, "Properties of Very Thin Aluminum Films," *Journal of Applied Physics*, vol. 42, pp. 51–53, Jan 1971.

[46] J. Martinis, "Thin critical field for completevortex expulsion from narrow superconducting strips," *Physical Review Letters*, vol. 92, no. 9, 2005.

[47] R. Gross, A. Marx, and F. Deppe, *Applied superconductivity: Josephson effect and superconducting electronics*. Walther-Meissner-Institut (WMI), Bayerische Akademie der Wissenschaften, Chair for Technical Physics (E23), Technische Universitaet Muenchen, Lecture Notes, 2015.

[48] C. W. J. Beenakker, "Universal limit of critical-current fluctuations in mesoscopic josephson junctions," *Phys. Rev. Lett.*, vol. 67, pp. 3836–3839, Dec 1991.

[49] T. Yokoyama, M. Eto, and Y. V. Nazarov, "Josephson current through semiconductor nanowire with spinorbit interaction in magnetic field," *Journal of the Physical Society of Japan*, vol. 82, no. 5, p. 054703, 2013.

[50] A. C. Doherty, T. W. Lynn, C. J. Hood, and H. J. Kimble, "Trapping of single atoms with single photons in cavity QED," *Physical Review A*, vol. 63, no. 1, p. 13401, 2000.

[51] J.-M. Raimond, M. Brune, and S. Haroche, "Manipulating quantum entanglement with atoms and photons in a cavity," *Reviews of Modern Physics*, vol. 73, no. 3, p. 565, 2001.

[52] H. Mabuchi and A. C. Doherty, "Cavity quantum electrodynamics: coherence in context," *Science*, vol. 298, no. 5597, pp. 1372–1377, 2002.

[53] K. Yoshida, K. Watanabe, and T. Kisu, "Evaluation of magnetic penetration depth and surface resistance of superconducting thin films using coplanar waveguides," *IEEE Transactions on*, 1995.

[54] S. Doyle, P. Mauskopf, J. Naylon, and A. Porch, "Lumped element kinetic inductance detectors," *Journal of Low*, 2008.

[55] R. Barends, "Photon-detecting superconducting resonators," 2009.

[56] A. Bruno, G. de Lange, S. Asaad, K. L. van der Enden, N. K. Langford, and L. DiCarlo, "Reducing intrinsic loss in superconducting resonators by surface treatment and deep etching of silicon substrates," *Applied Physics Letters*, vol. 106, p. 182601, May 2015.

[57] M. Khalil, M. Stoutimore, and F. Wellstood, "An analysis method for asymmetric resonator transmission applied to superconducting devices," *Journal of Applied*, 2012.

[58] P. d. Visser, "Quasiparticle dynamics in aluminium superconducting microwave resonators," 2014.

[59] Y. Makhlin, G. Schön, and A. Shnirman, "Quantum-state engineering with Josephson-junction devices," *Reviews of modern physics*, vol. 73, no. 2, p. 357, 2001.

[60] V. Bouchiat, D. Vion, P. Joyez, D. Esteve, and M. H. Devoret, "Quantum coherence with a single Cooper pair," *Physica Scripta*, vol. 1998, no. T76, p. 165, 1998.

[61] A. Blais, R.-S. Huang, A. Wallraff, S. M. Girvin, and R. J. Schoelkopf, "Cavity quantum electrodynamics for superconducting electrical circuits: An architecture for quantum computation," *Physical Review A*, vol. 69, no. 6, p. 62320, 2004.

[62] D. I. Schuster, A. A. Houck, J. A. Schreier, A. Wallraff, J. M. Gambetta, A. Blais, L. Frunzio, J. Majer, B. Johnson, M. H. Devoret, and Others, "Resolving photon number states in a superconducting circuit," *Nature*, vol. 445, no. 7127, pp. 515–518, 2007.

[63] M. H. Devoret and Others, "Quantum fluctuations in electrical circuits," *Les Houches, Session LXIII*, vol. 7, no. 8, 1995.

[64] A. Cottet, "Implementation of a quantum bit in a superconducting circuit," *PhD thesisUniversit{é} Paris VI*, vol. 14, 2002.

[65] L. S. Bishop, *Circuit Quantum Electrodynamics*. PhD thesis, Yale University, jul 2010.

[66] D. Vion, A. Aassime, A. Cottet, P. Joyez, H. Pothier, C. Urbina, D. Esteve, and M. H. Devoret, "Manipulating the quantum state of an electrical circuit," *Science*, vol. 296, no. 5569, pp. 886–889, 2002.

[67] E. T. Jaynes and F. W. Cummings, "Comparison of quantum and semiclassical radiation theories with application to the beam maser," *Proceedings of the IEEE*, vol. 51, no. 1, pp. 89–109, 1963.

[68] E. M. Purcell, "Spontaneous emission probabilities at radio frequencies," *Physical Review*, vol. 69, p. 681, 1946.

[69] K. S. A. Novoselov, A. K. Geim, S. Morozov, D. Jiang, M. Katsnelson, I. Grigorieva, S. Dubonos, and A. Firsov, "Two-dimensional gas of massless Dirac fermions in graphene," *nature*, vol. 438, no. 7065, pp. 197–200, 2005.

[70] T. W. Larsen, K. D. Petersson, F. Kuemmeth, T. S. Jespersen, P. Krogstrup, J. Nygaard, and C. M. Marcus, "Semiconductor-nanowire-based superconducting qubit," *Phys. Rev. Lett.*, vol. 115, p. 127001, Sep 2015.

[71] G. de Lange, B. van Heck, A. Bruno, D. J. van Woerkom, A. Geresdi, S. R. Plissard, E. P. A. M. Bakkers, A. R. Akhmerov, and L. DiCarlo, "Realization of microwave quantum circuits using hybrid superconducting-semiconducting nanowire Josephson elements," *Phys. Rev. Lett.*, vol. 115, p. 127002, Sep 2015.